

# 1 **senSCOPE: Modeling radiative transfer and biochemical processes in** 2 **mixed canopies combining green and senescent leaves with SCOPE**

3 Javier Pacheco-Labrador<sup>1</sup>, Tarek S. El-Madany<sup>1</sup>, Christiaan van der Tol<sup>2</sup>, M. Pilar Martin<sup>3</sup>, Rosario  
4 Gonzalez-Cascon<sup>4</sup>, Oscar Perez-Priego<sup>5</sup>, Jinhong Guan<sup>6</sup>, Gerardo Moreno<sup>7</sup>, Arnaud Carrara<sup>8</sup>, Markus  
5 Reichstein<sup>1</sup> and Mirco Migliavacca<sup>1</sup>.

6 <sup>1</sup>Max Planck Institute for Biogeochemistry, Hans Knöll Straße 10, Jena, D-07745, Germany

7 <sup>2</sup>Faculty of Geo-Information Science and Earth Observation (ITC), University of Twente, PO Box 217, AE  
8 Enschede 7500, The Netherlands

9 <sup>3</sup>Environmental Remote Sensing and Spectroscopy Laboratory (SpecLab), Institute of Economic, Geography and  
10 Demography (IEGD-CCHS), Spanish National Research Council (CSIC), C/Albasanz 26-28, 28037 Madrid,  
11 Spain

12 <sup>4</sup>Department of Environment, National Institute for Agriculture and Food Research and Technology (INIA), Ctra.  
13 Coruña, Km. 7,5, 28040 Madrid, Spain

14 <sup>5</sup>Department of Biological Sciences Macquarie University, 6 Wally's Walk, NSW 2109, Australia.

15 <sup>6</sup>State Key Laboratory of Soil Erosion and Dryland Farming on the Loess Plateau, Northwest A&F University,  
16 Yangling, Shaanxi 712100, China

17 <sup>6</sup>Forest Research Group - INDEHESA University of Extremadura, 10600 Plasencia, Spain

18 <sup>7</sup>Fundación Centro de Estudios Ambientales del Mediterráneo (CEAM), Charles Darwin 14, Parc Tecnològic,  
19 46980 Paterna, Spain

20 *Correspondence to:* Javier Pacheco-Labrador ([jpacheco@bgc-jena.mpg.de](mailto:jpacheco@bgc-jena.mpg.de))

21

22

## 23 **Abstract.**

24 Semi-arid grasslands and other ecosystems combine green and senescent leaves featuring different  
25 biochemical and optical properties, as well as functional traits. Knowing how these properties vary is  
26 necessary to understand the functioning of these ecosystems. However, differences between green and  
27 senescent leaves are not considered in recent models representing radiative transfer, heat, water and  
28 CO<sub>2</sub> exchange such as the Soil-Canopy Observation of Photosynthesis and Energy fluxes (SCOPE).  
29 Neglecting the contribution of senescent leaves to the optical and thermal signal of vegetation limits the  
30 possibilities to use remote sensing information for studying these ecosystems; as well as neglecting their

31 lack of photosynthetic activity increases uncertainty in the representation of ecosystem fluxes. In this  
32 manuscript we present senSCOPE as a step towards a more realistic representation of mixed green and  
33 senescent canopies. senSCOPE is a modified version of SCOPE model that describes a canopy  
34 combining green and senescent leaves with different properties and function. The model relies on the  
35 same numerical solutions than SCOPE, but exploits the linear nature of the scattering coefficients to  
36 combine optical properties of both types of leaf. Photosynthesis and transpiration only take place in  
37 green leaves; and different green and senescent leaf temperatures are used to close the energy balance.  
38 Radiative transfer of sun-induced fluorescence (SIF) and absorptance changes induced by the  
39 xanthophyll cycle action are also simulated. senSCOPE is evaluated against SCOPE both using  
40 synthetic simulations, forward simulations based on observations in a Mediterranean tree-grass  
41 ecosystem, and inverting dataset of ground measurements of reflectance factors, SIF, thermal radiance  
42 and gross primary production on a heterogeneous and partly senescent Mediterranean grassland. Results  
43 show that senSCOPE outputs vary quite linearly with the fraction of green leaf area, whereas SCOPE  
44 does not respond linearly to the effective leaf properties, calculated as the weighted average of green  
45 and senescent leaf parameters. Inversion results and pattern-oriented model evaluation show that  
46 senSCOPE improves the estimation of some parameters, especially chlorophyll content, with respect  
47 SCOPE retrievals during the dry season. Nonetheless, inaccurate knowledge of the optical properties of  
48 senescent matter still complicates model inversion. senSCOPE brings new opportunities for the  
49 monitoring of canopies mixing green and senescent leaves, and for improving the characterization of the  
50 optical properties of senescent material.

## 51 **1 Introduction**

52 Consistent monitoring of relevant vegetation properties is an essential step towards understanding the  
53 response of vegetation function (e.g., photosynthesis, transpiration) to changes in environment. Among  
54 others, photosynthetic performance and water use efficiencies are key elements to predict and  
55 understand vegetation responses to the climate change scenarios (e.g., elevated atmospheric CO<sub>2</sub>  
56 concentration, higher temperatures and altered water regimes) (IPCC 2014). However, current Land

57 Surface Models (LSM) predictions of these fluxes include large uncertainties (Friedlingstein et al.  
58 2014); partly due to inadequate representation of different processes as well as to the lack of knowledge  
59 of functional parameters describing plant function (e.g., maximum carboxylation rate ( $V_{cmax}$ ), maximum  
60 electron transport rate ( $J_{max}$ ) or the Ball-Berry stomatal sensitivity ( $m$ )) (Rogers 2014; Rogers et al.  
61 2016; Schaefer et al. 2012). Recent efforts of the Remote Sensing (RS) community have focused on the  
62 estimation of these parameters either using statistical approaches (Serbin et al. 2015; Silva-Perez et al.  
63 2018), or combining Radiative Transfer Models (RTM) with Soil-Vegetation-Atmosphere Models  
64 (SVAT) (Bayat et al. 2018; Camino et al. 2019; Dutta et al. 2019; Pacheco-Labrador et al. 2019; Zhang  
65 et al. 2014; Zhang et al. 2018), notably using the Soil-Canopy Observation Photosynthesis and Energy  
66 fluxes (SCOPE) model (van der Tol et al. 2009).

67 SCOPE represents radiative transfer of optical and thermal infrared radiation (TIR), in a homogeneous  
68 1-D canopy, which is coupled with an energy balance and a photosynthesis models predicting heat and  
69 water fluxes and carbon assimilation. SCOPE also propagates leaf level sun-induced chlorophyll  
70 fluorescence (SIF) emission and absorptance changes related with the activation of the xanthophyll  
71 cycle (Vilfan et al. 2018) to top of the canopy radiances. SCOPE uses Fluspect to model leaf optical  
72 properties (Vilfan et al. 2016; Vilfan et al. 2018) and combines 4 different canopy RTM representing  
73 outgoing radiation ( $RTM_o$ ), SIF ( $RFM_f$ , (van der Tol et al. 2016)), TIR emission ( $RTM_t$ ) and  
74 xanthophyll absorption ( $RTM_z$ , (Vilfan et al. 2018)) that rely on the four stream SAIL extinction and  
75 scattering coefficients model (Verhoef 1984). In addition, Yang and colleagues (2017) developed  
76 mSCOPE, an extension of SCOPE that uses a different numerical solution of the radiative transfer  
77 problem to represent 1-D but vertically heterogeneous canopies.

78 A current limitation of SCOPE is the lack of representation of within-canopy heterogeneity of  
79 vegetation properties, and specifically the separation of green and senescent leaves, which feature large  
80 differences in biophysical properties and function. When leaves senesce, flavonoids undergo enzymatic  
81 oxidation processes within the leaf producing diverse semiquinones and quinones which can suffer non-  
82 enzymatic secondary reactions with phenols, amino acids and proteins or other polyphenols (Pourcel et  
83 al. 2007; Taranto et al. 2017). The result is a heterogeneous mixture of complex brown polymers,

84 difficult to characterize *in vivo* and responsible of the yellow and brown tones that these leaves exhibit  
85 (Guyot et al. 1996; Pourcel et al. 2007). The characterization of the optical properties of these  
86 “senescent” or “brown” pigments of leaves were addressed by Jacquemoud (1988) using albino corn  
87 leaves; however, the authors stated that the characterization had to be improved. In fact, the absorption  
88 coefficients currently used by Prospect are usually attributed to F. Baret, via personal communication  
89 (e.g., (Féret 2009)). Thus, the characterization of senescent pigments is not as thoroughly documented  
90 as for other pigments (Feret et al. 2008; Féret et al. 2017; Jacquemoud and Baret 1990; Vilfan et al.  
91 2018), and their concentration is presented in arbitrary units due to the measurement technique used in  
92 their determination (Jacquemoud 1988). Also, when leaves further degrade their color changes (Kidnie  
93 et al. 2015), and some of their optical properties might vary with respect to those characterized and used  
94 by leaf-level RTM. For example, Melendo-Vega et al, (2018) suggested that overestimation of near  
95 infrared reflectance factors in a semi-arid grassland could be related to senescent material, and that this  
96 effect increased with its longevity.

97 Commonly used models such as PROSAIL (Jacquemoud et al. 2009), or more recently SCOPE, allocate  
98 all the pigments in a unique “effective” according to the averaged concentrations of the different leaves  
99 of the canopy. However, this approach does not adequately represent mixed canopies with varying  
100 fractions of green and senescent leaves. The presence of non-photosynthetic elements in the canopy has  
101 been already addressed in turbid medium RTM (Bach et al. 2001; Braswell et al. 1996; Wenhan 1993)  
102 and used to improve the estimation of biophysical parameters such as leaf area index (*LAI*) or  
103 chlorophyll concentration ( $C_{ab}$ ) or the fraction of absorbed photosynthetically active radiation (Houborg  
104 and Anderson 2009; Houborg et al. 2009; Houborg and McCabe 2016; Wenhan 1993). However,  
105 senescent and green leaves do not only feature different optical properties, but also different  
106 physiological processes. For example, senescent leaves present little or no chlorophyll content  
107 (Hörtensteiner 2006; Whitfield and Rowan 1974) so that they do not assimilate CO<sub>2</sub> through  
108 photosynthesis. Also, senescent leaves do not transpire water and lack of stomatal regulation. Senescent  
109 leaves can pose problems for the retrieval of biophysical variables if not adequately represented (Bacour  
110 et al. 2002; Houborg and Boegh 2008; Wang et al. 2005). Analogously, inadequate representation of

111 green and senescent leaf pools could also potentially induce uncertainties in the simulation of processes  
112 at canopy scale related to photosynthesis and transpiration. Finally, given that SCOPE is now widely  
113 used for retrieval of functional properties (Bayat et al. 2018; Camino et al. 2019; Dutta et al. 2019;  
114 Pacheco-Labrador et al. 2019; Zhang et al. 2014; Zhang et al. 2018), these uncertainties can propagate  
115 in the estimated parameters (Pacheco-Labrador et al. 2019). This fact may limit the application of recent  
116 approaches combining RTM and SVAT models for the study of canopies or ecosystems featuring large  
117 fractions of dry leaves (in particular in grasslands or semi-arid ecosystems) or for the monitoring of  
118 vegetation health, crop productivity and phenology.

119 Senescent material is present in all vegetation, and for a remote sensing perspective is very critical for  
120 annual plants such as grasslands (Houborg et al. 2009; Melendo-Vega et al. 2018), which cover about  
121 40% of the Earth's terrestrial surface (Anderson 2006). Grassland's phenology and function are strongly  
122 governed by water availability, temperature, herbivory, fire, nitrogen deposition or CO<sub>2</sub> concentration  
123 increase (Anderson 2006; Cleland et al. 2006; Figueroa and Davy 1991; Luo et al. 2018; Migliavacca et  
124 al. 2011; Richardson et al. 2013). Green plants transit to senescent, recently dead, and long-term dead  
125 plants, each of them featuring different biophysical and optical properties (Kidnie et al. 2015). This  
126 transition varies with meteorology (Ren and Zhang 2018), biophysical properties (Henry et al. 2008;  
127 Sanaullah et al. 2010; Yuan and Chen 2009), plant functional types (Henry et al. 2008) and changes for  
128 different parts of the plant (Henry et al. 2008; Koukoura et al. 2003). Usually, even in grasses, leaves  
129 fall while stems stay longer and degrade more slowly due to differences in biochemical composition.  
130 Therefore, in multi-species grasslands senescence and degradation can take place at different rates and  
131 periods, increasing the variability of surface biophysical and optical properties as well as the complexity  
132 of modeling and characterization. In fact, senescent material and litter are nowadays considered a  
133 challenge for the estimation of biophysical properties in semi-arid grasslands (He and Mui 2010).

134 In this work, we present senSCOPE, a modified version of the SCOPE model that separates RTM and  
135 physiological processes (photosynthesis and transpiration) for green and senescent leaves. senSCOPE  
136 aims at improving the representation of radiative transfer and physiology in senescent canopies. The  
137 model is then evaluated in three ways:

138 1) We run a sensitivity analysis comparing forward simulations of SCOPE and senSCOPE under  
139 different meteorological conditions and under different combinations of vegetation parameters for  
140 different abundances of senescent leaves.

141 2) We use observations of model parameters and meteorological data at ecosystem scale to predict  
142 fluxes and compare them with EC data.

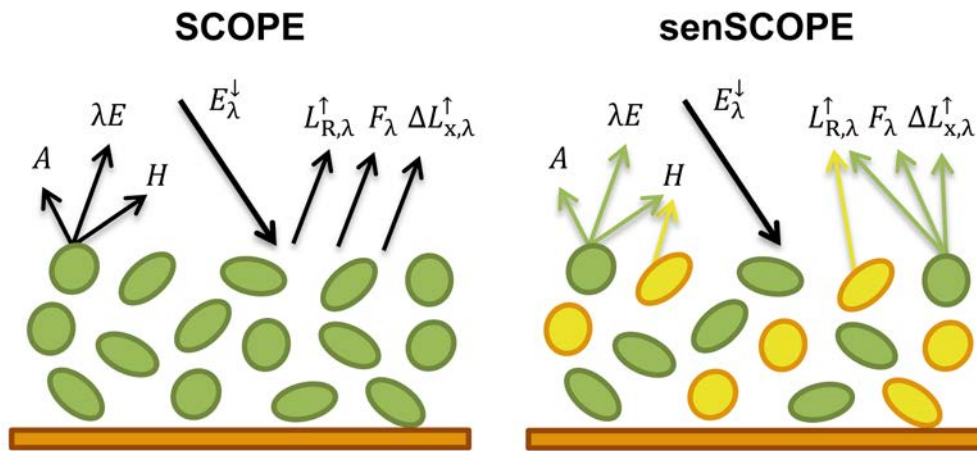
143 3) We invert SCOPE and senSCOPE against the same dataset of ground observations of carbon  
144 fluxes, reflectance factors ( $R$ ), SIF and TIR radiance used by Pacheco-Labrador et al, (2019) for  
145 comparison.

146 As in the former work, functional and biophysical model parameters are estimated by inverting SCOPE  
147 against different combinations of the abovementioned variables sampled at plot scale in a  
148 Mediterranean grassland. New inversion boundaries are used according to observations of some of the  
149 parameters in the site. Results of both inversions are compared and evaluated using pattern-oriented  
150 model evaluation approach (Pacheco-Labrador et al. 2019).

## 151 **2. Description of senSCOPE**

152 The model senSCOPE extends the 1-D model SCOPE to describe homogeneous canopies combining  
153 green and senescent leaves randomly mixed. Fig. 1 summarizes the conceptual differences between  
154 SCOPE and senSCOPE. Green leaves contain chlorophylls and other photosynthetic pigments that  
155 allow them to photosynthesize; and regulate their temperature via transpiration. In contrast, senescent  
156 leaves only contain senescent pigments and neither photosynthesize nor transpire. These leaves present  
157 some microbial activity related to its degradation, and superficial water (e.g., intercepted rainfall) can  
158 evaporate from their surface; however these processes are not represented neither by SCOPE nor  
159 senSCOPE. In senSCOPE, the leaf RTM Fluspect (Vilfan et al. 2016; Vilfan et al. 2018) simulates  
160 reflectance, transmittance and, in the case of green leaves, also fluorescence according to the  
161 biochemical and structural properties of each leaf type. Canopy RTM<sub>0</sub> implemented in SCOPE (van der  
162 Tol et al. 2009) is modified to separately compute the radiation absorbed by each leaf type; and the

163 energy balance model is customized to account for the presence of leaves that neither photosynthesize  
164 nor transpire. Since green and senescent leaves feature different radiative balances, a modified RTM<sub>t</sub>  
165 model quantifies thermal emission of each of these two leaf types separately and combines them  
166 according to the corresponding fractions of leaf area ( $f$ ); then the model calculates scattering and  
167 absorption of this diffuse flux. Eventually, fluorescence emission and optical changes induced by the  
168 activation of the xanthophyll cycle in the green leaves is propagated to top of canopy (TOC) radiances  
169 and  $R$  using the RTM<sub>f</sub> (van der Tol et al. 2016) and RTM<sub>z</sub> (Vilfan et al. 2018) models already  
170 implemented in SCOPE. Both models are coded in Matlab (Matwoks Inc., Natick, MA, USA).



171

172 **Figure 1. Conceptual differences between SCOPE and senSCOPE models. Green and yellow colours**  
173 **correspond to green and senescent leaves, respectively. Black arrows show processes featured by all leaves;**  
174 **whereas coloured arrows refer to processes featured only for a given type of leaf. The scheme represents**  
175 **assimilation ( $A$ ), latent ( $\lambda E$ ) and sensible heat ( $H$ ) fluxes, incoming spectral irradiance ( $E_{\lambda}$ ), reflected**  
176 **spectral radiance ( $L_{R,\lambda}$ ), emitted fluorescence radiance ( $F_{\lambda}$ ) and changes in  $L_{R,\lambda}$  due to activation of**  
177 **xanthophyll cycle ( $\Delta L_{x,\lambda}$ )**

178 senSCOPE relies on the same solution of the radiative transfer problem implemented in SCOPE, since it  
179 exploits the linear nature of the single leaf scattering efficiency factors (Verhoef 1984) to combine the  
180 optical properties of green and senescent leaves in an “averaged” leaf. This is simple if leaf angle  
181 distribution is assumed the same for both types of leaves. The main advantage of this approach is that it  
182 allows representing physiological processes separately in each leaf type. This is important since  
183 photosynthesis and transpiration are non-linearly related with radiation and leaf temperature, and



184 therefore might not be adequately represented by a model featuring a unique leaf type characterized by  
185 the “averaged parameters” of photosynthetic and non-photosynthetic leaves.

186 senSCOPE requires a larger number of parameters than SCOPE, since two different leaves must be  
187 described, as well as their respective area fractions. Alternatives to minimize the number of parameters  
188 and simplify the application of the model in inverse problems are presented in Sect. 3.2.2 and discussed  
189 later.

## 190 **2.1 Radiation Fluxes**

191 As SCOPE, senSCOPE relies on SAIL 4-stream theory that can be summarized by a system of four  
192 linear equations describing the radiative transfer of the solar direct flux ( $E_s$ ), the downward diffuse flux  
193 ( $E^-$ ), the upward diffuse flux ( $E^+$ ), and the flux in the observation direction ( $E_o$ ).

$$194 \quad \frac{dE_s}{Ldx} = kE_s, \quad (1a)$$

$$195 \quad \frac{dE^-}{Ldx} = -sE_s + aE^- - \sigma E^+, \quad (1b)$$

$$196 \quad \frac{dE^+}{Ldx} = -s'E_s + \sigma E^- - aE^+, \quad (1c)$$

$$197 \quad \frac{dE_o}{Ldx} = wE_s + vE^- + v'E^+ - KE_o, \quad (1a)$$

198 In this system,  $x$  represents the vertical relative height within the canopy ( $x = 0$  for top,  $x = -1$  for  
199 bottom), and  $L$  represents the Leaf Area Index (also  $LAI$ ). The remaining variables are the SAIL  
200 coefficients defined for first time by Verhoef (1984).  $k$  and  $K$  are the extinction coefficients in the solar  
201 and observation directions, respectively. They depend on the sun-view geometry,  $LAI$  and the leaf angle  
202 distribution ( $LAD$ ); and they are therefore independent of leaf optical properties.  $s$ ,  $a$ ,  $\sigma$ ,  $s'$ ,  $w$ ,  $v$  and  $v'$   
203 are the scattering coefficients depending on sun-view geometry, canopy structure and leaf optical  
204 properties. These coefficients define the relationship between a given incident flux ( $E_1$ ) and a given  
205 scattered flux ( $E_2$ ) in the canopy, and they are computed by integrating single-leaf scattering efficiency  
206 factors ( $Q_{sc}$ ) that represent the analogous relationship for individual leaves. The scattering coefficient



207 (b) corresponding to all the leaves of given zenith inclination angle ( $\theta_1$ ) can be defined as (Verhoef  
208 1984):

$$209 \quad b(\theta_1) = \frac{L'}{2\pi} \int_0^{2\pi} Q_{sc}(E_1, E_2) d\varphi_1, \quad (2)$$

210 where  $L'$  is the LAI contained in a horizontal layer of the canopy of width  $dx$  and  $\varphi_1$  is the leaf azimuth  
211 angle.

212 As in SCOPE, senSCOPE solves the radiative transfer problem numerically, defining a discrete number  
213 of canopy layers and leaf angles.  $Q_{sc}(E_1, E_2)$  are defined assuming that individual leaves are Lambertian  
214 diffusors of known hemispherical reflectance ( $\rho$ ) as and hemispherical transmittance ( $\tau$ ).  $\rho$  and  $\tau$  are  
215 predicted in SCOPE by Fluspect (Vilfan et al. 2016). For each pair of incident and scattered fluxes,  
216  $Q_{sc}(E_1, E_2)$  is defined as a linear combination of  $\rho$  and/or  $\tau$  weighted by spectrally invariant factors  
217 determined by the geometry of the leaf, or more specifically, the projection of the leaves with respect to  
218 the incident flux ( $E_1$ ) and the downward (-) or upward (+) scattered flux ( $E_2$ ). As proposed by Bach et  
219 al, (2001), senSCOPE exploits this linear nature of  $Q_{sc}$  to combine the  $\rho$  and the  $\tau$  of green and  
220 senescent leaves into an averaged factors; weighted by their corresponding fractions of leaf area (Eq. 3  
221 and 4). This approach allows applying the solution already proposed by van der Tol et al., (2009) for the  
222 linear system shown in Eq. 1a-d.

$$223 \quad \rho = f_{\text{green}}\rho_{\text{green}} + (1 - f_{\text{green}})\rho_{\text{senes}}, \quad (3)$$

$$224 \quad \tau = f_{\text{green}}\tau_{\text{green}} + (1 - f_{\text{green}})\tau_{\text{senes}}, \quad (4)$$

225 where subscripts “green” and “senes” indicate the type of leaf. Notice that the weighted average of  $\rho$   
226 and  $\tau$  is not equivalent to the factors predicted for a weighted average of the leaf parameters.

227 This approach is suitable to represent the radiative transfer of a canopy of homogeneously mixed green  
228 and senescent leaves. In order to represent physiological processes for each leaf type separately, it is  
229 necessary differentiating the amount total radiation absorbed by each leaf type, and the  
230 photosynthetically active radiation ( $PAR$ ) absorbed by chlorophyll ( $E_{\text{ap,Chl}}$ ). SCOPE quantifies  $E_{\text{ap,Cab}}$   
231 ( $\text{W m}^{-2}$ ) using the relative absorption of this pigment respect to the remaining total absorption in the leaf

232 in each spectral band ( $k_{\text{Chl,rel}}$ ).  $E_{\text{ap,Chl}}$  is computed for the direct ( $E_{\text{ap,Chl,dir}}$ ) and the diffuse irradiances  
 233 ( $E_{\text{ap,Chl,dif}}$ ) as follows:

$$234 \quad E_{\text{ap,Chl,dir}} = f_{\text{green}} \int_{\lambda=400}^{\lambda=700} k_{\text{Chl,rel,green}}(\lambda) E_{\text{sun}}(\lambda) [1 - \rho_{\text{green}}(\lambda) - \tau_{\text{green}}(\lambda)] d\lambda, \quad (5)$$

$$235 \quad E_{\text{ap,Chl,dif}}(x) = f_{\text{green}} \int_{\lambda=400}^{\lambda=700} k_{\text{Chl,rel,green}}(\lambda) [E^-(x, \lambda) + E^+(x, \lambda)] [1 - \rho_{\text{green}}(\lambda) - \tau_{\text{green}}(\lambda)] d\lambda, \quad (6)$$

236 where  $\lambda$  is the wavelength and  $k_{\text{Chl,rel,green}}$  is  $k_{\text{Chl,rel}}$  in the green leaves. These quantities are calculated  
 237 from the upward and downward fluxes without modifying the transfer of radiation. Since senSCOPE  
 238 defines senescent leaves as containing no chlorophyll,  $k_{\text{Chl,rel}} = 0$  in senescent leaves and for this reason,  
 239 absorbed PAR used to simulate photosynthesis in sunlit ( $E_{\text{ap,Chl,u}}$ ) and shaded leaves ( $E_{\text{ap,Chl,h}}$ ) per total  
 240 leaf area of the mixed canopy scales with  $f_{\text{green}}$ . Shaded leaves (subscript ‘h’) are only illuminated by  
 241 diffuse light (Eq. 7); whereas Eq. 5 and 6 must be combined to get  $E_{\text{ap,Chl}}$  in the sunlit leaves ( $E_{\text{ap,Chl,u}}$ ,  
 242 subscript ‘u’) (Eq. 8).

$$243 \quad E_{\text{ap,Chl,h}}(x) = E_{\text{ap,Chl,dif}}(x), \quad (7)$$

$$244 \quad E_{\text{ap,Chl,u}}(x, \theta_1, \varphi_1) = |f_s(x, \theta_1, \varphi_1)| E_{\text{ap,Chl,dir}} + E_{\text{ap,Chl,dif}}(x), \quad (8)$$

245 where  $f_s$  is a geometric factor accounting for the projection of each leaf towards the sun.

246 Total absorbed radiation is used to compute the radiation budget in the canopy and determines leaf  
 247 temperature, which has implications for photosynthesis and transpiration, and must therefore be  
 248 computed separately for each leaf type. Total absorbed radiation is computed by SCOPE similarly as in  
 249 Eq. 5-8, but integrating the fluxes in the full spectral domain (e.g., 400-50.000 nm):

$$250 \quad E_{a,i,dir} = f_i \int_{\lambda=400}^{\lambda=50000} E_{\text{sun}}(\lambda) [1 - \rho_i(\lambda) - \tau_i(\lambda)] d\lambda, \quad (9)$$

$$251 \quad E_{a,i,dif}(x) = f_i \int_{\lambda=400}^{\lambda=50000} [E^-(x, \lambda) + E^+(x, \lambda)] [1 - \rho_i(\lambda) - \tau_i(\lambda)] d\lambda, \quad (10)$$

$$252 \quad E_{a,i,h}(x) = E_{a,i,dif}(x) \quad (11)$$

$$253 \quad E_{a,i,u}(x, \theta_1, \varphi_1) = |f_s(x, \theta_1, \varphi_1)| E_{a,i,dir} + E_{a,i,dif}(x), \quad (12)$$

254 Where subscript “i” now stands for either ‘green’ or ‘senescent’.

## 255 2.2 Energy balance

256 As in SCOPE, energy balance is closed iteratively by modifying canopy and soil temperatures until the  
257 following is met for the soil and for all leaf angles and layers separately:

$$258 |R_n - H - \lambda E - G| < \varepsilon_{\text{threshold}}, \quad (13)$$

259 where  $R_n$  is net radiation,  $H$  is latent heat flux,  $\lambda E$  is energy heat flux,  $G$  is soil heat flux and  $\varepsilon_{\text{threshold}}$  is a  
260 predefined threshold for the accepted energy balance closure error ( $\varepsilon_{\text{threshold}}$ ), all in  $\text{W m}^{-2}$ .

261 senSCOPE addresses the energy balance separating the processes occurring in green and senescent  
262 leaves, where only the first are assumed to photosynthesize and transpire. Therefore,  $\varepsilon_{\text{ebal}}$  is separated  
263 into the following elements (Eq. 14):

$$264 R_{n,\text{green}} - R_{n,\text{senes}} - R_{n,\text{soil}} - H_{\text{green}} - H_{\text{senes}} - H_{\text{soil}} - \lambda E_{\text{green}} - \lambda E_{\text{soil}} - G = \varepsilon_{\text{ebal}}, \quad (14)$$

265 where the subscript “soil” refers to soil fluxes, and only green leaves and soil contribute to  $\lambda E$ .  
266 However, notice that similarly as in SCOPE, the energy balance is separately closed for soil and for all  
267 leaf angles, layers and leaf types.

268 In order to compute  $R_n$ , the contribution of thermal emission must be added to the absorbed radiation  
269 calculated in Sect. 2.1. senSCOPE separately represents the temperatures of green and senescent leaves  
270 ( $T_{c,\text{green}}$ ,  $T_{c,\text{senes}}$ , respectively) since they absorb radiation cool down differently. Distinguishing these  
271 temperatures has an impact on the calculation of photosynthesis, which is temperature dependent.  
272 Consequently, black-body thermal emission ( $H_c$ ) is different for each leaf type ( $H_{c,\text{green}}$ ,  $H_{c,\text{senes}}$ ); and the  
273 on-sided black-body thermal emission of all leaves is computed as a linear combination of the emission  
274 of each leaf type in the canopy:

$$275 \varepsilon H_c = f_{\text{green}} \varepsilon_{\text{green}} H_{c,\text{green}}(T_{c,\text{green}}) + (1 - f_{\text{green}}) \varepsilon_{\text{senes}} H_{c,\text{senes}}(T_{c,\text{senes}}), \quad (15)$$

276 where  $\varepsilon$  is the emissivity, and equals absorptance ( $1 - \rho - \tau$ ) according to Kirchhoff’s Law. The propagation  
277 of emitted radiation by leaves and soil through the canopy is calculated using the averaged layer  
278 properties as in the original SCOPE. In order to quantify the net thermal radiation (emitted minus

279 absorbed) ( $R_{n,t}$ ) senSCOPE calculates the amount of energy absorbed by each leaf type using their  
280 respective emissivity:

$$281 \quad R_{n,t,green} = [E^- + E^+ - 2H_{green}] \varepsilon_{green} f_{green} , \quad (16)$$

$$282 \quad R_{n,t,senes} = [E^- + E^+ - 2H_{senes}] \varepsilon_{senes} (1 - f_{green}) , \quad (17)$$

283 where  $E^-$  and  $E^+$  are the diffuse emitted fluxes.  $R_{n,t}$  of sunlit and shaded leaves is computed  
284 separately. These are energy fluxes per total (senescent plus green) leaf surface area. Therefore, canopy  
285 net radiation is computed as the addition of  $E_a$  and  $R_{n,t}$ ; and  $R_{n,t} = R_{n,t,green} + R_{n,t,senes}$  without the need to  
286 further weight by fraction.

287 Aerodynamic resistances are computed as in SCOPE for the whole mixed canopy, since they depend on  
288 meteorology and canopy structure. Consequently water and heat fluxes ( $H_{green}$ ,  $H_{senes}$  and  $\lambda E_{green}$ ) in  
289 senSCOPE are computed with an identical representation of resistances as in SCOPE, but with leaf  
290 temperatures differentiated per leaf type. These fluxes are defined per unit of leaf-type surface, and need  
291 to be scaled to the fraction of  $LAI$  represented by each leaf type in the mixed canopy. Eventually,  
292 senSCOPE iteratively resolves six temperatures: sunlit and shaded green leaves ( $T_{c,u,green}$ ,  $T_{c,h,senes}$ ),  
293 sunlit and shaded senescent leaves ( $T_{c,u,senes}$ ,  $T_{c,h,usenes}$ ), and both sunlit and shaded soil ( $T_{s,u}$ ,  $T_{s,h}$ ).

### 294 **2.3 Photosynthesis**

295 In senSCOPE, only green leaves photosynthesize and transpire. Photosynthesis is driven by the  $PAR$   
296 absorbed by chlorophyll ( $APAR_{Chl}$ ; which equals  $E_{ap,Chl}$  transformed from  $W m^{-2}$  to  $\mu mol m^{-2} s^{-1}$ ). The  
297 absorbed  $PAR$  by chlorophyll in green leaves per unit green leaf area is  $E_{ap,Chl,green} = E_{ap,Chl} / f_{green}$ . Other  
298 area-based inputs such as maximum carboxylation rate  $V_{cmax}$  [ $\mu mol m^{-2} s^{-1}$ ], as well as model outputs  
299 (e.g., internal  $CO_2$  concentration,  $C_i$  [ $\mu mol m^{-3}$ ]) refer to green leaves only. Assimilation ( $A_c$ ) is  
300 therefore initially computed per unit green leaf area. The stomatal conductance ( $r_{cw}$ ) as output of the  
301 leaf biochemical model is further used to calculate the transpiration of green leaves  $\lambda E_{green}$ , also per unit  
302 green leaf area. Consequently, both fluxes first calculated per unit green leaf area, and later scaled with  
303  $f_{green}$ .

## 304 **2.4 Fluorescence**

305 SCOPE computes leaf level fluorescence emission using three main elements: incident irradiance in the  
306 excitation range 400-750 nm, excitation-fluorescence (E-F) matrices ( $M(\lambda_e, \lambda_f)$  and  $M'(\lambda_e, \lambda_f)$  for  
307 backwards and forward fluorescence, respectively), and the amplification factors  $\Phi'_f$  which are  
308 provided by the biochemical model for sunlit and shaded leaves. E-F matrices represent the excitation  
309 of chlorophyll and the radiative transfer of incident and re-emitted radiation inside the leaf (Vilfan et al.  
310 2016). In senSCOPE the leaf fluorescence emission is only calculated for green leaves, because for  
311 senescent leaves, the E-F matrices equal zero. Then the emission is scaled with  $f_{\text{green}}$ .

$$312 E_1^f = f_{\text{green}} \cdot \Phi'_f \cdot [(M'_{\text{green}}(\lambda_e, \lambda_f) + M_{\text{green}}(\lambda_e, \lambda_f))] \otimes E, \quad (18)$$

313 Leaf level fluorescence emission is then propagated to top of the canopy combining the same radiative  
314 transfer approach used by SCOPE and the averaged leaf optical properties ( $\rho$  and  $\tau$ ) for the mixed  
315 canopy.

## 316 **2.5 Xanthophyll cycle**

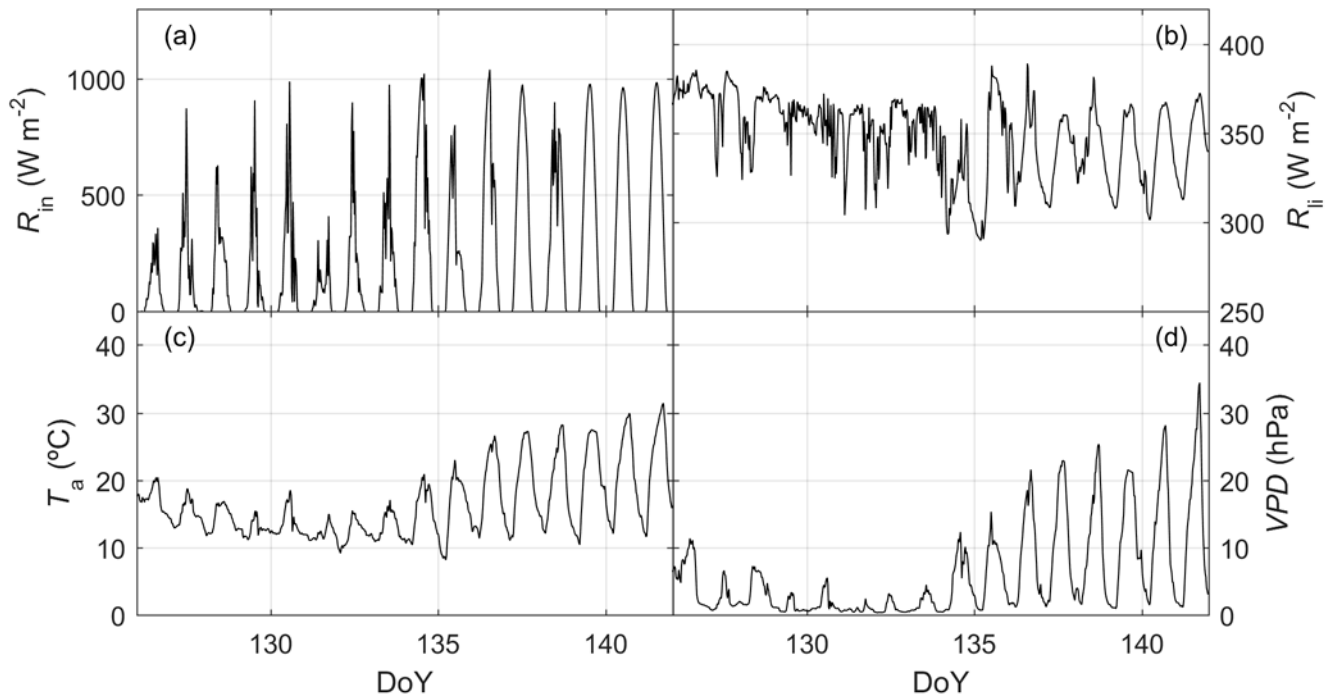
317 A recent version of SCOPE incorporates Fluspect-CX (Vilfan et al. 2018), a leaf RTM that simulates  
318 the variations in leaf optical properties induced by the activation of the xanthophyll cycle for  
319 photosynthetic down-regulation-, and propagates these variations from leaf to canopy level radiances.  
320 Changes in leaf optical properties are computed after photosynthesis, as a function of the rate  
321 coefficient for non-photochemical quenching ( $K_n$ ) provided by the biochemical module. This rate serves  
322 as a scaling factor of leaf  $\rho$  and  $\tau$  between two extreme cases of with completely activated and  
323 completely deactivated xanthophyll cycle. In senSCOPE, senescent leaves show no carotenoids, no  
324 xanthophyll cycle and no related changes in optical properties; for this reason, the extreme cases  
325 calculated on the averaged  $\rho$  and  $\tau$  simulate only variations induced by the green leaves.  $K_n$  is a rate  
326 defining the probability of the different fates of photons exciting chlorophyll, therefore, and similarly to  
327  $\Phi'_f$ , it does not require additional correction. Therefore, senSCOPE uses the same radiative transfer  
328 functions than SCOPE for the propagation of signals related with the xanthophyll cycle.

## 329 3. Methods

### 330 3.1 Comparison with SCOPE model. Sensitivity analysis

331 In order to evaluate the differences between senSCOPE and the original model SCOPE (van der Tol et  
332 al. 2009), we run two different series of forward simulations modifying separately meteorological  
333 variables ( $F_{\text{meteo}}$ ) and vegetation properties ( $F_{\text{veg}}$ ). Eleven different canopies with  $f_{\text{green}}$  ranging between  
334 0.0 and 1.0 with steps of 0.1 were simulated. As input to SCOPE we used weighted averages of the leaf  
335 parameters of each leaf type; similarly as field leaf measurements would be averaged to calculate  
336 canopy mean values.

337 In order to provide realistic meteorological forcing in the simulations  $F_{\text{meteo}}$ , we used actual  
338 measurements acquired in the research site of Majadas de Tiétar between 5<sup>th</sup> and the 20<sup>th</sup> May 2016  
339 (day of the year (DoY) 126 and 141, respectively). Fig. 2 summarizes this dataset.



340

341 **Figure 2. Short wave (a) and long wave incoming radiation (b), air temperature (c) and vapour pressure**  
342 **deficit (d) recorded in Majadas de Tiétar between the 5<sup>th</sup> and the 20<sup>th</sup> May 2019 (DoY 126 and 141,**  
343 **respectively) used in the forward simulation  $F_{\text{meteo}}$ .**

344 Short wave incoming radiation ( $R_{\text{in}}$ ,  $\text{W m}^{-2}$ ), long wave incoming radiation ( $R_{\text{li}}$ ,  $\text{W m}^{-2}$ ), air temperature  
345 ( $T_{\text{a}}$ ,  $^{\circ}\text{C}$ ), atmospheric vapour pressure ( $e_{\text{a}}$ , hPa), wind speed ( $u$ ,  $\text{m s}^{-1}$ ), air pressure ( $p$ , hPa) and soil  
346 moisture ( $SM_{\text{p}}$ , % volume) were provided by a sub-canopy eddy covariance station at 1.6 m height  
347 (detailed description of the system can be found in El-Madany et al, (2018) and Perez-Priego et al,  
348 (2017)). Vapour pressure deficit ( $VPD$ , hPa) was calculated from  $T_{\text{a}}$  and  $e_{\text{a}}$ ; also, soil resistance for  
349 evaporation from the pore space ( $r_{\text{ss}}$ ,  $\text{s m}^{-1}$ ) was estimated as a function of using  $SM_{\text{p}}$  the model SCOPE  
350 v1.73. Sun zenith ( $\theta_{\text{s}}$ ) and azimuth ( $\varphi_{\text{s}}$ ) angles were computed from timestamps and site location. In the  
351  $F_{\text{meteo}}$  runs, only the abovementioned variables were modified; leaf and canopy properties were kept  
352 constant for the different  $f_{\text{green}}$  levels tested. Only daytime data ( $\theta_{\text{s}} < 85.0$  deg) were used in the  
353 simulation; which equals 422 runs per model and  $f_{\text{green}}$  level.

354  $F_{\text{veg}}$  represented varying vegetation properties under constant meteorological conditions. To do so, we  
355 selected midday conditions of the 18<sup>th</sup> May 2019 (DoY 139). A look up table with 500 samples of  $C_{\text{ab}}$ ,  
356 carotenoids concentration ( $C_{\text{ca}}$ ),  $V_{\text{cmax}}$ , Fluorescence quantum efficiency ( $f_{\text{qe}}$ ),  $m$  and  $LAI$  was generated  
357 using Latin Hypercube Sampling (McKay et al. 1979).  $C_{\text{ca}}$  and  $V_{\text{cmax}}$  were constrained as a function of  
358  $C_{\text{ab}}$  mimicking the relationships (linear function and noise) reported in Sims and Gamon (2002) and  
359 Croft et al, (2017), respectively. Table 1 shows the ranges of variation generated for each parameter  
360 varying in each  $F_{\text{veg}}$  simulation. Additionally, a smaller dataset was generated modifying only  $LAI$  or  
361  $C_{\text{ab}}$  (and  $V_{\text{cmax}}$  and  $C_{\text{ca}}$  as a function of these) to illustrate an example of the response of models to these  
362 parameters. Several model outputs and internal parameters were evaluated. Moreover, we also  
363 compared the predicted underlying water use efficiency ( $uWUE$ , Eq. 19):

$$364 \quad uWUE = \frac{A}{\lambda E_{\text{c}}} \sqrt{VPD}, \quad (19)$$

365 where  $\lambda E_{\text{c}}$  is the canopy  $\lambda E$ , excluding evaporation from the soil.

366



367

368 **Table 1. Vegetation parameters used in the forward simulation  $F_{veg}$ .**

Parameter	Symbol	Units	Range
Leaf chlorophyll content	$C_{ab}$	$\mu\text{g cm}^{-2}$	[0.13, 99.98]
Leaf carotenoids content	$C_{ca}$	$\mu\text{g cm}^{-2}$	[0.02, 37.26]
Maximum carboxylation capacity	$V_{cmax}$	$\text{mmol m}^{-2} \text{s}^{-1}$	[0.40, 162.78]
Ball-Berry sensitivity parameter	m	-	[0.05, 39.98]
Fluorescence quantum efficiency	$f_{qe}$	-	[0.01, 0.03]
Leaf area index	LAI	$\text{m}^2 \text{m}^{-2}$	[0.00, 7.99]

369

370 The Matlab<sup>TM</sup> Profiler (Matwoks Inc., Natick, MA, USA) was used to evaluate the computing time and  
371 number of calls of the different functions of each model used during these simulations in each run.  
372 These metrics, together with the total computation time and the number of unsuccessful runs -where the  
373 energy balance does not succeed to converge to a solution-, were used to compare models'  
374 performances.

### 375 **3.2 Comparison with SCOPE model. Forward simulation with observational datasets**

376 SCOPE and senSCOPE were also run forward using observational datasets from the study site of  
377 Majadas de Tiétar, Cáceres, Spain (39° 56' 24.68"N, 5° 45' 50.27"W). Observations -and when missing  
378 estimates- of vegetation properties and forcing variables integrated at ecosystem scale were used to run  
379 both models. Predicted fluxes and reflectance factors where compared with EC observations and  
380 hyperspectral airborne imagery.

### 381 3.2.1 Study site and datasets

382 The study site is located in the experimental station of Majadas de Tiétar. It is a managed tree-grass  
383 ecosystem combining sparse trees (*Quercus ilex* L. subsp. *ballota* [Desf.] Samp) and a highly diverse  
384 herbaceous cover combining numerous species of three main functional plant forms: grasses, forbs and  
385 legumes. The climate is continental Mediterranean so that the grassland shows a strong seasonality  
386 initiated by greening phase around April, followed by a dry season that starts between May and June, a  
387 second re-greening driven by autumn rains, and a dormant phase during winter (El-Madany et al. 2018).  
388 The grassland phenology and functioning strongly responds to light and temperature in spring and to  
389 water availability in late spring-summer and in autumn (Luo et al. 2018). Several species grow and  
390 senesce at different times, usually, in early spring senescent material remnant from the winter is already  
391 present, then new material is also generated during spring, where  $f_{\text{green}}$  can already be already as low as  
392  $\sim 0.7$  (Melendo-Vega et al. 2018).

393 In this site, three EC towers monitor three areas of the same ecosystem, one of them fertilized with  
394 nitrogen (N) and another one with N plus phosphorous (P), and the control one with no fertilization.  
395 These towers include also eddy covariance systems around 15 m above the ground, providing  
396 ecosystem-level measurements of carbon and water fluxes. Three sub-canopy towers monitor grassland  
397 fluxes  $\sim 1.6$  m aboveground. Details of the instrumentation and the manipulation can be found in El-  
398 Madany et al, (2018) and Perez-Priego et al, (2017). Also, a series of airborne campaigns with the  
399 Compact Airborne Spectrographic Imager CASI-1500i (Itres Research Ltd., Calgary, AB, Canada),  
400 operated by the Instituto Nacional de Técnica Aeroespacial (INTA) were conducted between 2012 and  
401 2017. From a total of 17 images, a  $R$  of the footprint of each EC tower and campaign was extracted.  
402 Details of methods and data processing can be found in Pacheco-Labrador et al., (2017). Additionally,  
403 in each of the airborne campaigns, destructive sampling of vegetation provided estimates of ecosystem  
404  $LAI$ ,  $f_{\text{green}}$ ,  $C_{\text{dm}}$ ,  $C_{\text{w}}$ , Nitrogen concentration ( $N_{\text{mass}}$ ) and/or  $C_{\text{ab}}$  and  $C_{\text{ca}}$ . Further information on protocols  
405 and methods can be found in Melendo-Vega et al., (2018), Gonzalez-Cascon et al., (2017) and  
406 (Gonzalez-Cascon and Martin 2018).

### 407 **3.2.2 senSCOPE and SCOPE. Forward simulation and evaluation**

408 Observed/estimated forcing variables and vegetation properties were used to predict fluxes and  
409 reflectance factors  $\pm 1$  day around each flight campaign in each EC tower during daytime. Since no field  
410 observations of all the vegetation parameters were available, some of them had to be estimated. When  
411 missing,  $C_{ab}$  and  $C_{ca}$  were estimated from their relationship with  $N_{mass}$  observed in the site. Also  $V_{cmax}$   
412 was estimated as a function of  $N_{mass}$  in the green leaves ( $N_{mass,green}$ ) following the relationship in Feng  
413 and Dietze (2013), and assumed  $45 \mu\text{mol m}^{-2} \text{s}^{-1}$  for tree leaves. A constant  $m$  parameter of 10 was  
414 assumed,  $N$  and  $LAD$  were assumed 1.5 and spherical, respectively.  $C_s$  was estimated from the  
415 remaining leaf parameters inverting the statistical model described section 3.3.2 and in Appendix A.  
416 Soil reflectance was determined by  $SM_p$  and the parameters estimated by inversion of the BSM model  
417 (Verhoef et al. 2018) in Pacheco-Labrador et al (2019). Also,  $r_{ss}$  was estimated as function of  $SM_p$   
418 using the model in Pacheco-Labrador et al (2019).

419 Then, we evaluated the capability of both models to predict  $GPP$ ,  $\lambda E$ ,  $R_n$ ,  $G$ , and  $H$  comparing SCOPE  
420 and senSCOPE predictions with EC fluxes in the site. We also evaluated model performance and  
421 structure using predicted fluxes and computing quantities that describe energy partitioning, the  
422 evaporative fraction (Eq. 20)

$$423 \quad EF = \frac{\lambda E}{\lambda E + H}, \quad (20)$$

424 where  $\lambda E$  and  $H$  are the total latent heat sensible heat fluxes, respectively.

425 Emitted irradiance in the TIR ( $E_t$ ) was compared with net radiometer measurements in the EC towers  
426 (CNR4, Kipp and Zonen, Delft, Netherlands); also  $R$  were compared with those of the imagery at the  
427 time of the overpass.

### 428 **3.3 Comparison with SCOPE model. Inversion on observational datasets**

429 In order to assess the impact of accounting for senescence material during the estimation of key  
430 biophysical (e.g.,  $LAI$ ,  $C_{ab}$ ) and functional (e.g.,  $V_{cmax}$ ,  $m$ ) vegetation parameters, we compared the  
431 parameter estimates and posterior predictions resulting from the inversion of both models against real

432 observations in a Mediterranean grassland in the context of a nutrient manipulation experiment with N  
433 and P, featuring  $f_{\text{green}}$  between 0.05-1. In this work, we inverted SCOPE and senSCOPE using the  
434 inversion method and approaches proposed in Pacheco-Labrador et al. (2019).

### 435 **3.3.1 Study site and datasets**

436 The inversion the models is tested using field observations from the understory grass layer of the site of  
437 Majadas de Tiétar, Cáceres, Spain, acquired in the context of the Small-scale MANipulation  
438 Experiment (SMANIE) (Perez-Priego et al. 2015). This manipulation nutrient experiment was  
439 performed in an open area to minimize the effect of trees. The experimental design consisted of 4  
440 blocks (4 replicates each) with N, P, both (NP) additions, and the control treatment (C, not fertilized).  
441 As a result of the fertilization, N, NP and P treatments induced changes in plant community, plant  
442 structure and function (Martini et al. 2019; Migliavacca et al. 2017; Perez-Priego et al. 2015). 9 field  
443 campaigns took place between 2014-2016 covering spring and early summer. In each block, midday  
444 measurements were carried out in two different collars with a dual spectroradiometric system providing  
445 hyperspectral  $R$  and SIF estimates in the O<sub>2</sub>-A ( $F_{760}$ ) and the O<sub>2</sub>-B ( $F_{687}$ , not in all the campaigns).  
446 Diurnal time course of TIR up-welling radiance ( $L_t$ ) and  $GPP$  was determined using gas exchange  
447 chambers from sunrise to sunset. Fluxes were collected quasi-simultaneously in the same collars of the  
448 radiometric measurements at midday. The mismatch between the radiometric and chamber  
449 measurements was minimum. Moreover, destructive sampling near by the collars provided estimates of  
450 plant traits ( $f_{\text{green}}$ ,  $LAI$ , and nitrogen concentration  $N_{\text{mass}}$ ). Additional information about instrumentation,  
451 sampling methods and data processing can be found elsewhere (Martini et al. 2019; Migliavacca et al.  
452 2017; Pacheco-Labrador et al. 2019; Perez-Priego et al. 2015).

### 453 **3.2.2 senSCOPE and SCOPE. Inversion and evaluation**

454 We inverted senSCOPE and SCOPE using the same datasets and methodology described for the  
455 inversion of SCOPE in Pacheco-Labrador et al. (2019). Observations of  $R$  and  $L_t$ ,  $F_{760}$  and/or  $GPP$  were  
456 used to estimate  $LAI$ ,  $C_{\text{ab}}$ ,  $V_{\text{cmax}}$ ,  $m$  and other biophysical parameters (Table 2) using an innovative  
457 methodology that combined biophysical and functional constraints in two different steps. Three

458 different sets of constraints (inversion schemes) were tested, each combined in the first step of the  
 459 inversion (Step#1), noon  $R$  with noon  $GPP$  ( $I_{GPP}$ ), noon  $GPP$  and  $F_{760}$  ( $I_{GPP-SIF}$ ), or nothing else ( $I_R$ ).

460 **Table 2. Parameters estimated inverting senSCOPE model**

Parameter	Symbol	Units	Step	Inversion bounds
Leaf chlorophyll content	$C_{ab}$	$\mu\text{g cm}^{-2}$	#1	[0, 100]
Leaf carotenoids content	$C_{ca}$	$\text{Mg cm}^{-2}$	#1	[0, 40]
Senescent material	$C_s$	-	#1	[0, 7.5]
Leaf water content	$C_w$	$\text{g cm}^{-2}$	#1	$[6.3 \cdot 10^{-5}, 0.06]$
Leaf dry matter content	$C_{dm}$	$\text{g cm}^{-2}$	#1	[0.0019, 0.03]
Leaf structural parameter	N	Layers	#1	[1, 3.6]
Leaf area index	LAI	$\text{m}^2 \text{m}^{-2}$	#1	[0, 8]
Leaf inclination distribution function	$LIDF_a$	-	#1	[-1, 1]; $ LIDF_a + LIDF_b  \leq 1$
Bimodality of the leaf inclination	$LIDF_b$	-	#1	
Maximum carboxylation capacity	$V_{cmax}$	$\mu\text{mol m}^{-2} \text{s}^{-1}$	#1 & #2	[0, 200]
Ball-Berry sensitivity parameter	$m$	-	#2	[0, 50]
Fluorescence quantum efficiency	$f_{qe}$	-	#1 & #2	[0,1]

461

462 In Step#1 biophysical parameters of the SCOPE model and a first guess of  $V_{cmax}$  were estimated.  
 463 Uncertainties were estimated using a Bayesian approach (Omlin and Reichert 1999). Then, in a second  
 464 step (Step#2) the guess of  $V_{cmax}$  was used as a prior and diel cycles of  $L_t$  combined with diel  $GPP$  ( $I_{GPP}$ ),  
 465 diel  $GPP$  and noon  $F_{760}$  ( $I_{GPP-SIF}$ ), or only diel  $L_t$  ( $I_R$ ) were used to estimate the functional parameters  
 466  $V_{cmax}$  and  $m$ .  $f_{qe}$  was estimated in both steps in the schemes  $I_{SIF}$  and  $I_{GPP-SIF}$ . Also, pattern-oriented model  
 467 evaluation was used to assess the results of the different schemes. Unlike the previous work, this time

468 we increased the inversion bounds (Table 2) for  $C_{dm}$  and  $C_w$  according to observed distributions in the  
469 site (Martín et al. 2019; Melendo-Vega et al. 2018). Also, since previous works found problems to  
470 cover the range of  $R$  in the near infrared,  $C_s$  upper bound was raised up to 7.5 a.u.; a value that allowed  
471 covering the low  $R$  values found in dry periods in the ecosystem (Martín et al. 2019). The multiple  
472 constraint inversion approach proposed in Pacheco-Labrador et al. (2019) provided coherent parameter  
473 estimates when  $GPP$  constrained the inversion ( $I_{GPP}$  and  $I_{GPP-SIF}$ ) using SCOPE; however, uncertainties  
474 in part related to the presence of senescent materials biased the estimation some of the parameters,  
475 notably  $C_{ab}$  during the dry season. In all the cases senescent material also was suspected to induce  
476 underestimation of  $LAI$ .

477 We used the same methodology to invert senSCOPE on the same datasets in order to compare the  
478 results provided by both models and to understand the suitability of using senSCOPE in environments  
479 featuring large fractions of senescent leaves. However, in the case of senSCOPE, 6 leaf parameters of  
480 two different leaf types must be estimated (Table 2). In order limit the number of free parameters in the  
481 inversion, we applied the following constraints: We assumed that green leaves presented no senescent  
482 pigments ( $C_s = 0$ ) whereas senescent leaves only presented senescent pigments ( $C_{ab} = C_{ca} = 0$ ). We also  
483 assumed that the mesophyll parameter ( $N$ ) and dry matter content ( $C_{dm}$ ), were the same for both types of  
484 leaves, whereas that water content ( $C_w$ ) of green leaves was four times higher than senescent  $C_w$  (Kidnie  
485 et al. 2015). This allowed us reducing the degrees of freedom by 6. We assumed that average leaf  
486 parameters ( $X$ ) could be computed as a linear combination of the parameters of each leaf type ( $X_{green}$  and  
487  $X_{senes}$ ) as in Eq. 21:

$$488 \quad X = X_{green} \cdot f_{green} + X_{senes} \cdot (1 - f_{green}), \quad (21)$$

489 Given the constrains imposed on leaf parameters, we could directly optimize the leaf averaged  
490 parameters in the inversion, similarly as parameters are retrieved in the inversion of SCOPE (Pacheco-  
491 Labrador et al. 2019). To do so,  $X_{green}$  or  $X_{senes}$  are internally calculated solving them from Eq. 21; which  
492 is possible in all the cases since at least the value one of them together with  $f_{green}$  are known: Either they  
493 are equal, 0, or their ratio has been prescribed. senSCOPE includes the additional parameter  $f_{green}$ ; in  
494 order to reduce equifinality and as well as the number of parameters to estimate we prescribed  $f_{green}$  by

495 modelling it as a function of the averaged leaf parameters  $X$  using a Neural Network (NN). The NN was  
496 trained from a look up table of individual  $X_{\text{green}}$  and  $X_{\text{senes}}$  parameters averaged as a function of  $f_{\text{green}}$ ; no  
497 assumptions on  $N$ ,  $C_w$  and  $C_{\text{dm}}$  were made (Appendix A). As a result, the same parameters were  
498 estimated in the inversion of SCOPE and senSCOPE.

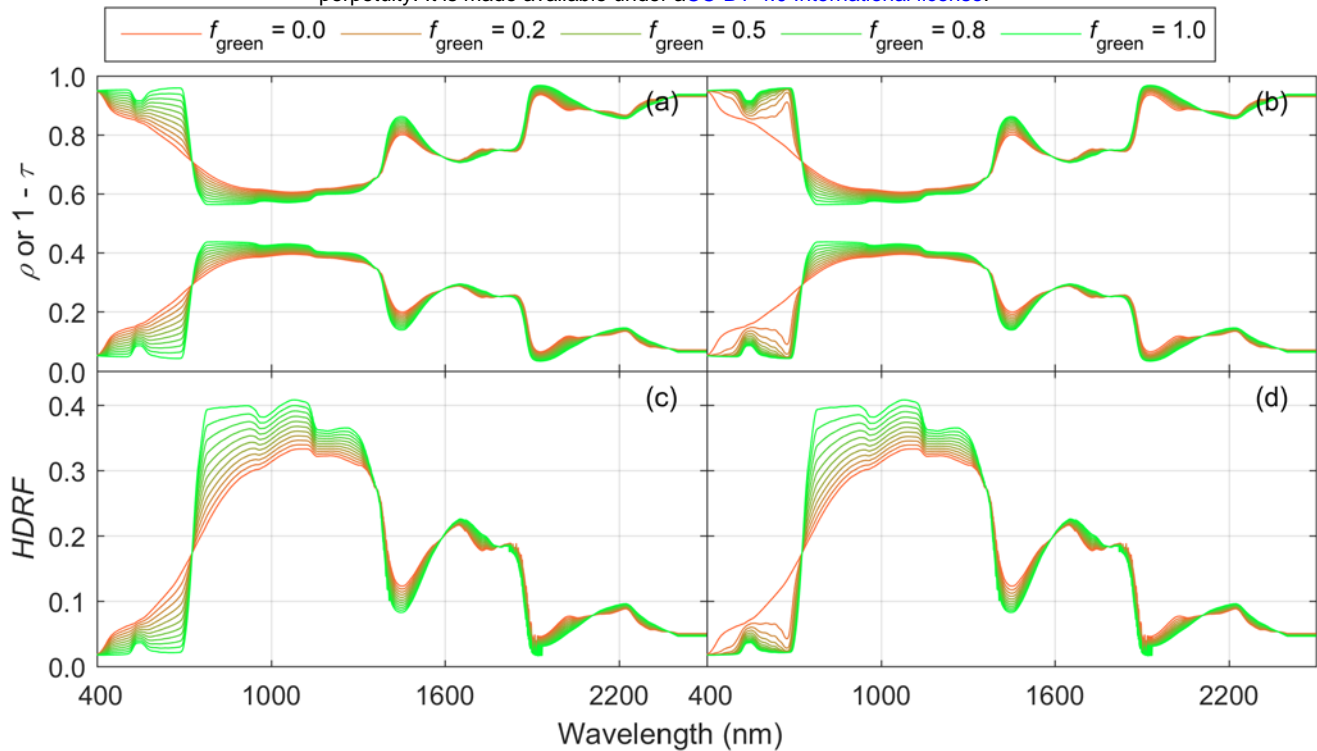
499 As in Pacheco-Labrador et al. (2019), we used pattern-oriented model evaluation approach to assess the  
500 retrieval of functional parameters, which cannot be determined from individual leaf measurements in  
501 the highly biodiverse grassland under study. To do so, we assessed the relationship of  $V_{\text{cmax}}$  and  $C_{\text{ab}}$   
502 against  $N_{\text{mass}}$  in the green fraction of the canopy ( $N_{\text{mass,green}}$ ), and in the case of  $V_{\text{cmax}}$  it was compared  
503 with the relationship published by Feng and Dietze (2013) for grasslands. We also evaluated model  
504 performance and structure using not directly predicted fluxes, but variables derived from them such as  
505  $EF$ , which describes energy partitioning (Eq. 19). In addition, a more traditional evaluation was also  
506 done assessing the goodness of the fit or prediction of model constraints ( $R$ ,  $L_t$ ,  $F_{760}$ , and/or  $GPP$ ) and  
507 observed parameters ( $LAI$ ,  $f_{\text{green}}$ ).

## 508 **4. Results**

### 509 **4.1 Comparison of results and performance with SCOPE model: Sensitivity analysis.**

510 For the  $F_{\text{meteo}}$  runs, green and senescent leaf properties were kept constant for the different combinations  
511 of  $f_{\text{green}}$ . Fig. 3a,b show the leaf optical properties simulated with senSCOPE and SCOPE, respectively.  
512 Accordingly Fig. 3c,d shows the TOC Hemispherical-Directional Reflectance Factors ( $HDRF$ )  
513 simulated with each model at midday of DoY 139, the timestamp used for  $F_{\text{veg}}$  runs. As can be seen,  
514 senSCOPE predicts spectroradiometric variables that vary more proportionally to  $f_{\text{green}}$ , whereas SCOPE  
515 simulates stronger absorptions, especially in the visible region. This results from allocating all the  
516 absorptive substances to a single leaf type. The largest differences between models are found in the red  
517 and blue regions, where senescent leaves in senSCOPE increase scattering. We also verified that when  
518  $f_{\text{green}}$  equals 1 or 0, the output of both models is the same.



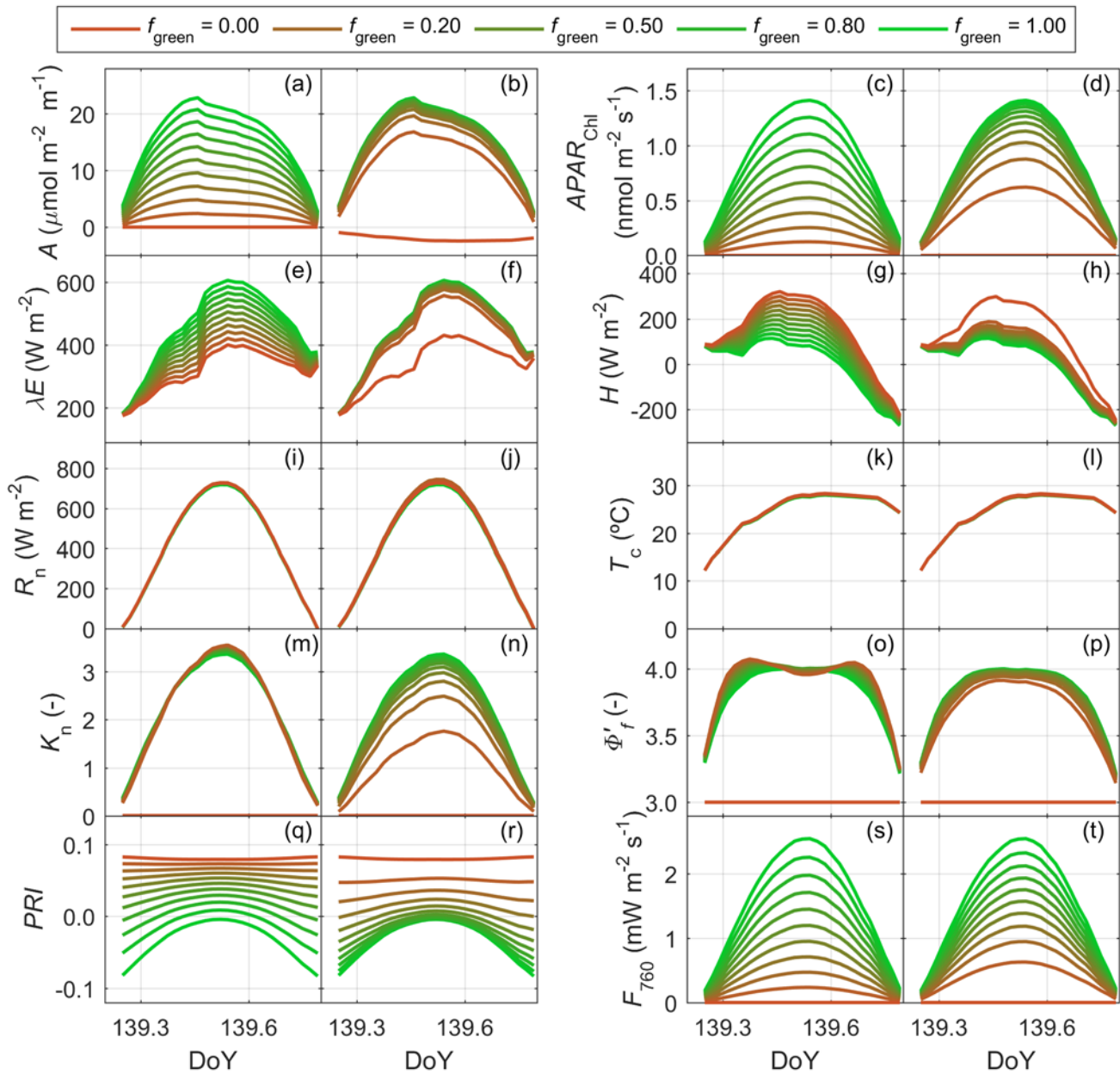


519

520 **Figure 3. Leaf reflectance and transmittance factors predicted by senSCOPE (a) and SCOPE (b); and top**  
 521 **of the canopy Hemispherical Directional Reflectance Factors predicted by senSCOPE (c) and SCOPE (d)**  
 522 **for different fractions of green and senescent leaves.**

523 Fig. 4 compares some of the spectroradiometric variables and fluxes predicted by senSCOPE (left semi-  
 524 columns) and SCOPE (right semi-columns) during DoY 139 in the  $F_{\text{meteo}}$  runs. As can be seen, those  
 525 variables that are strongly controlled by radiative transfer in the optical domain ( $APAR_{\text{chl}}$  (Fig. 4c,d),  
 526 the Photochemical Reflectance Index ( $PRI$ , Gamon et al, (1992)), sensitive to activation of the  
 527 xanthophyll cycle (Fig. 4q,r) and  $F_{760}$  (Fig. 4s,t)) present a stronger and more linear sensitivity to  $f_{\text{green}}$ .  
 528 The same is observed for the water and energy fluxes ( $\lambda E$  (Fig. 4e,f) and  $H$  (Fig. 4g,h)). Differences for  
 529 variables related with the radiative transfer of thermal radiance seem to be lower ( $R_n$  (Fig. 4i,j) and  $T_c$   
 530 (Fig. 4k,l)). senSCOPE leaves feature a higher absorption of  $PAR$  per unit green leaf area, which  
 531 produces a stronger NPQ activation ( $K_n$  (Fig. 4m,n)), and a depletion of photosynthetic efficiency  
 532 around midday ( $\Phi'_f$  (Fig. 4o,p)) for low  $f_{\text{green}}$  (unlike the other parameters, these are only representative  
 533 of green leaves). Notice that the example shown is only representative of the meteorological and

534 vegetation properties represented during DoY 139, and the differences shown should not be taken  
 535 generally.

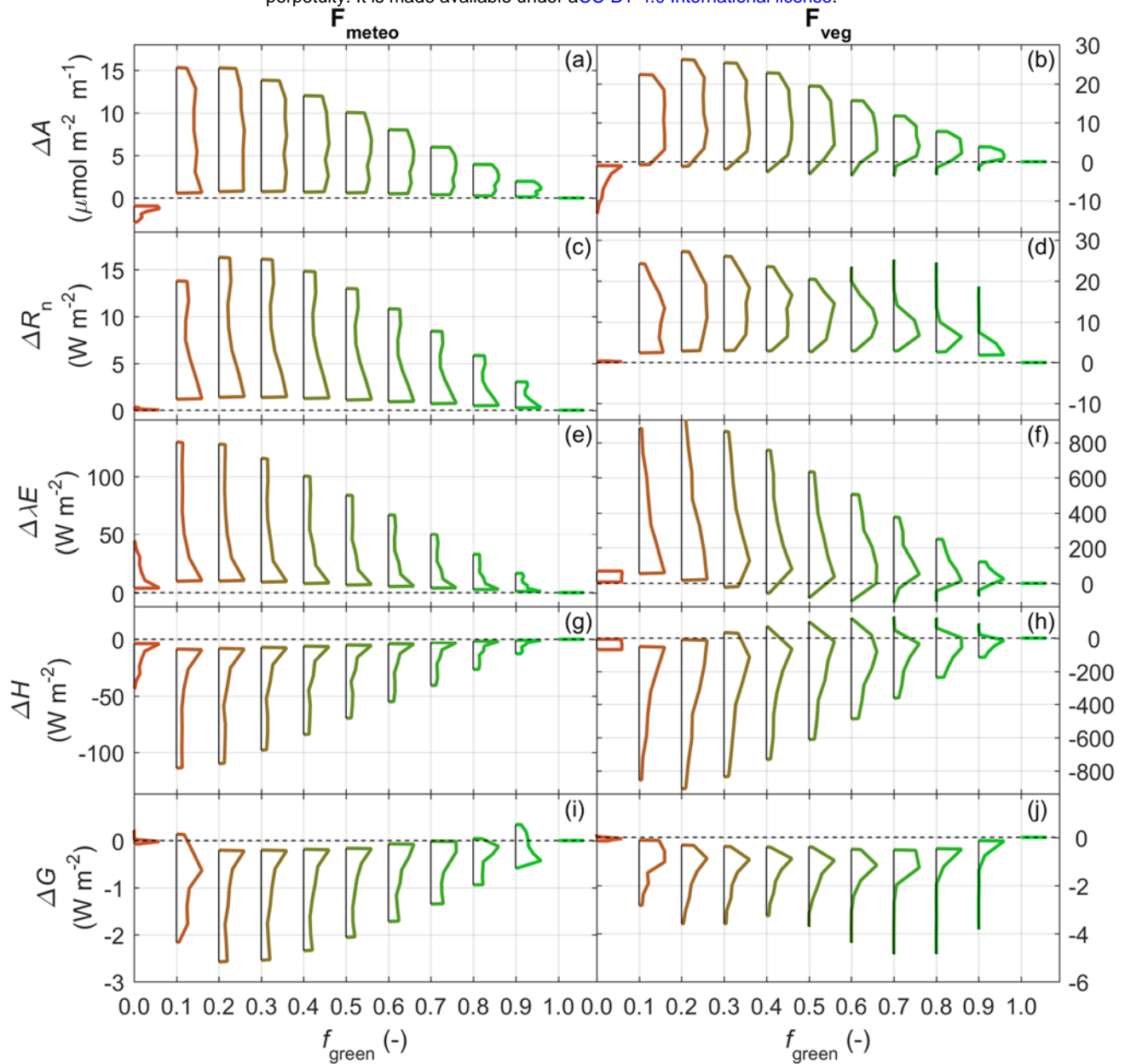


536

537 **Figure 4. Diel cycles of senSCOPE (left semi-column) and SCOPE (right semi-column) predicted variables**  
 538 **on DoY 136: Assimilation (a,b), photosynthetically active radiation absorbed by chlorophylls (c,d), latent**  
 539 **and sensible heat fluxes (g,h), net radiation (i,j), canopy temperature (k,l), rate coefficient for non-**

540 **photochemical quenching (m,n), fluorescence efficiency (o,p), photochemical reflectance index (q,r) and**  
541 **TOC fluorescence radiance at 760 nm (s,t).**

542 Fig. 5 shows the distributions of the difference between fluxes predicted by SCOPE and (minus)  
543 senSCOPE for each  $f_{\text{green}}$  level. Results of the  $F_{\text{meteo}}$  and the  $F_{\text{veg}}$  simulations are shown in the left and  
544 the right columns, respectively. As can be seen, both under varying meteorological conditions and  
545 varying plant properties, the two models predict the same fluxes when  $f_{\text{green}} = 1$ , but not always when  
546  $f_{\text{green}} = 0$ . For  $f_{\text{green}} < 1$  SCOPE predicts higher assimilation ( $A$ , Fig. 5a,b); but in the case of  $f_{\text{green}} = 0$ ,  
547 where SCOPE predicts negative  $A$  due to photorespiration, and senSCOPE represents no photosynthetic  
548 leaf area. SCOPE also predicts in most of the cases higher  $R_n$  (Fig. 5c,d) and  $\lambda E$  (Fig. 5e,f), and lower  $H$   
549 (Fig. 5g,h) and  $G$  (Fig. 5i,j).



550

551 **Figure 5. Distributions of the difference between the fluxes simulated with SCOPE and (minus) senSCOPE**  
552 **in the  $F_{\text{meteo}}$  run (left column) and the  $F_{\text{veg}}$  run (right column) for different fractions of green leaf area:**  
553 **assimilation (a,b), net radiation (c,d), latent heat flux (e,f), sensible heat flux (g,h) and soil heat flux (i,j).**

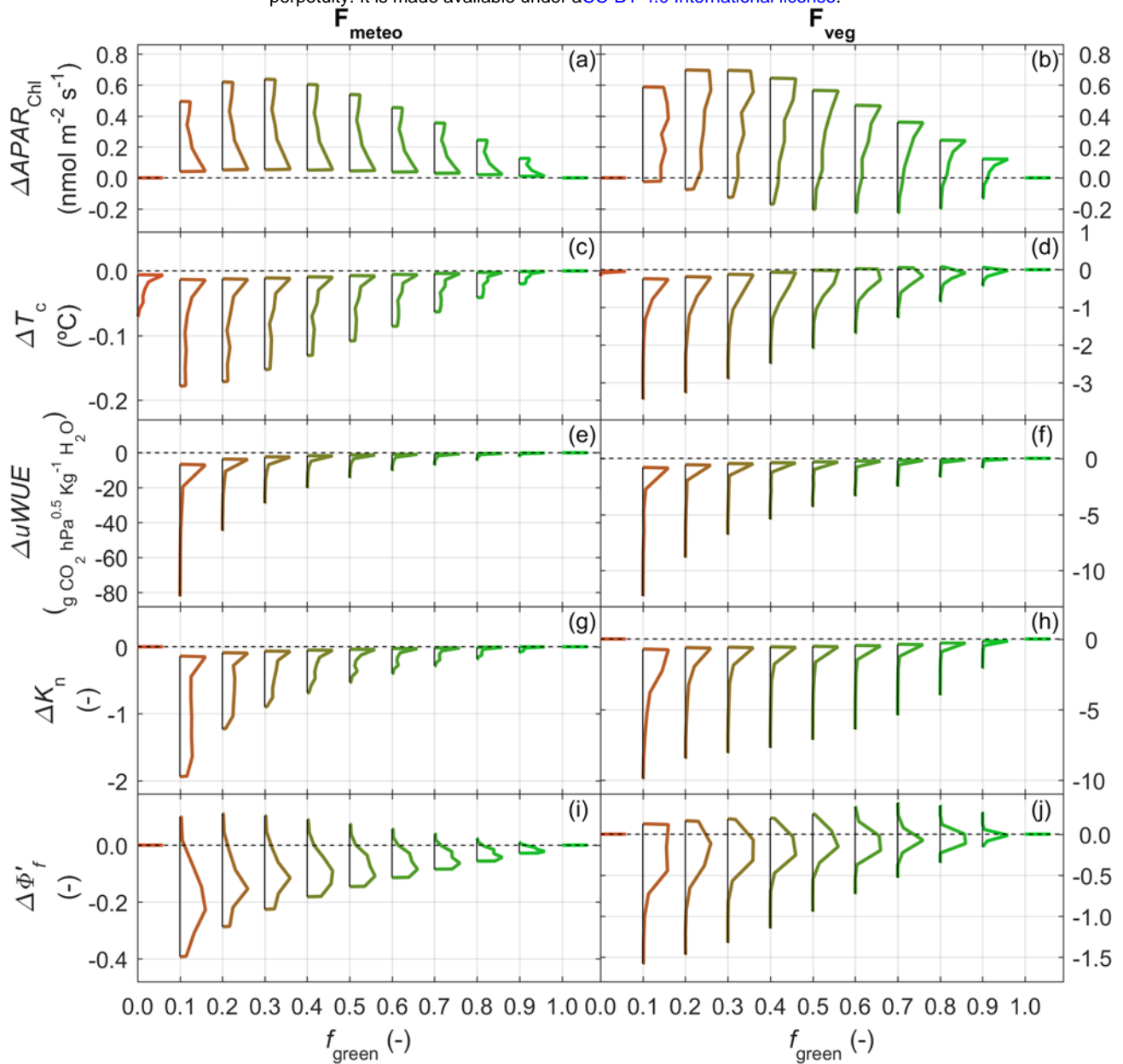
554

555

556 Differences between predicted fluxes usually maximize when  $C_{ab}$  and  $LAI$  increase (Fig. S1a-e and S2  
557 a-e, respectively).  $G$  (and  $R_n$ ) also present large differences for low values of these parameters and mid  
558  $f_{green}$ . In the analysis of the forward runs, the differences observed from  $F_{veg}$  simulations are often larger  
559 than those  $F_{meteo}$  simulations since the variability in the meteorological variables is -in relative terms-  
560 lower than the variability simulated for the vegetation properties.

561 For each  $f_{green}$  level, Fig. 6 presents the distribution of the difference between variables related to leaf  
562 function, as predicted by SCOPE and (minus) senSCOPE. Results of  $F_{meteo}$  and  $F_{veg}$  are shown on the  
563 left and the right columns, respectively. Similar to the fluxes, these variables are integrated according to  
564  $LAI$  and the probability of each sunlit and shaded leaf angle.  $APAR_{Chl}$  (Fig. 6a,b) is equal for both  
565 models when the canopy is totally green or senescent. For the rest of the cases SCOPE predicts higher  
566  $APAR_{Chl}$ , except some cases when  $C_{ab} < 10 \mu g cm^{-2}$  (not shown). senSCOPE predicts higher canopy  
567 temperature ( $T_c$ , Fig. 6c,d) than SCOPE; the largest differences are found when  $C_{ab}$  is high (Fig. S1g),  
568 or when  $LAI$  is low (Fig. S2g). Similarly,  $uWUE$  (Fig. 6e,f) is higher for senSCOPE, but unlike  $T_c$  and  
569 most of the variables compared, differences in  $uWUE$  are more strongly controlled by meteorological  
570 conditions than by vegetation parameters. The largest differences in  $uWUE$  are found under cold  
571 conditions with  $VPD < 5$  hPa (not shown). senSCOPE presents also higher  $K_n$  (Fig. 6g,h). Differences  
572 between models predictions increase with  $LAI$  (Fig. S2i), and decrease with  $C_{ab}$  (Fig. S1i).  $\Phi'_f$  (Fig. 5i,j)  
573 is most often higher for senSCOPE than for SCOPE, especially if  $LAI$  is high and  $C_{ab}$  is low (not  
574 shown). On the other hand, SCOPE predicts higher  $\Phi'_f$  when  $LAI$  is low (Fig. S2j) or when  $C_{ab}$  is low  
575 and  $LAI$  is moderate (Fig. S1j). As expected, both models predict the same values for these variables  
576 when  $f_{green} = 1$ .

577



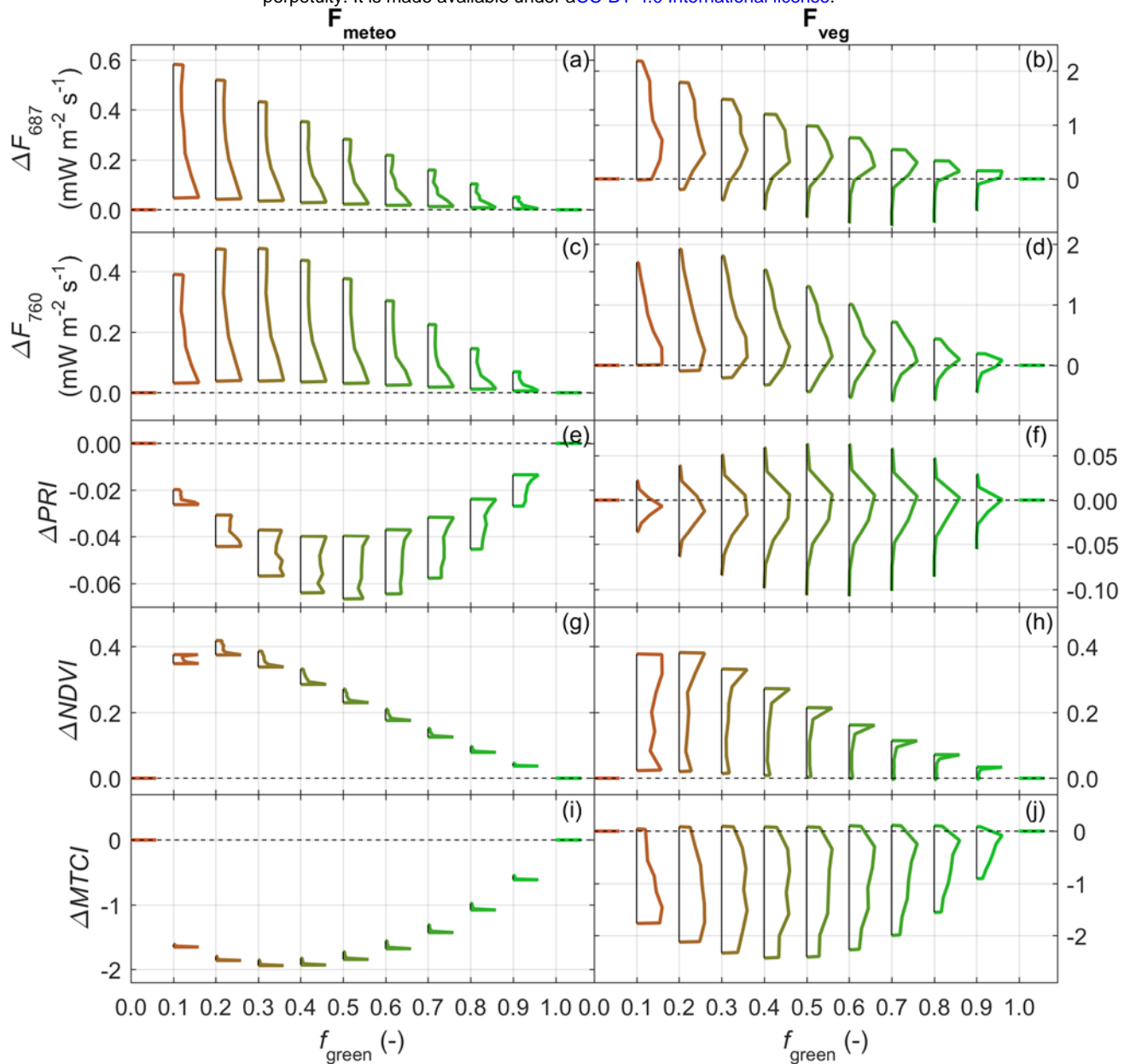
578

579 **Figure 6. Distributions of the difference between variables indicative of plant physiology simulated with**  
 580 **SCOPE and (minus) senSCOPE in the  $F_{\text{meteo}}$  run (left column) and the  $F_{\text{veg}}$  run (right column) for different**  
 581 **fractions of green leaf area: photosynthetically active radiation absorbed by chlorophylls (a,b), canopy**  
 582 **temperature (c,d), underlying water use efficiency (e,f), rate coefficient for non-photochemical quenching**  
 583 **(g,h) and fluorescence efficiency (i,j).**

584 Fig. 7 shows the distribution of some TOC spectroradiometric variables predicted by SCOPE and  
585 (minus) senSCOPE for each  $f_{\text{green}}$  level. Results of the  $F_{\text{meteo}}$  and the  $F_{\text{veg}}$  simulations are presented in the  
586 left and the right columns, respectively.  $F_{687}$  (Fig. 7a,b) and  $F_{760}$  (Fig. 7c,d) are larger for SCOPE in  
587 most of the cases; the largest differences are found for low  $f_{\text{green}}$  and large  $C_{\text{ab}}$  (Fig. S1k,l) and  
588 LAI (Fig. S2k,l). Differences in  $PRI$  are negative for  $F_{\text{meteo}}$ , but of both signs for  $F_{\text{veg}}$  (Fig. 7e,f). In  
589 this case, the influence of vegetation parameters is more complex and less linear than in other variables;  
590 since it depends on the combination of  $C_{\text{ab}}$  and  $C_{\text{ca}}$ , their ratio and  $LAI$  (not shown). A similar analysis  
591 carried out on the  $PRI$  computed from reflectance factors where the effect of the xanthophyll cycle is  
592 not simulated reveals that differences between models rather respond to biophysical properties than to  
593 differences in function (not shown). Two more spectral indices responsive to pigments content and  
594 canopy structure are also analysed. Fig. 7g,h presents the differences for the Normalized Difference  
595 Vegetation Index ( $NDVI$ , Rouse et al, (1974)); Fig. 7i,j present differences for the MERIS Terrestrial  
596 Chlorophyll Index ( $MTCI$ , Dash and Curran (2007)); senSCOPE predicts lower and higher values,  
597 respectively. For these indices, the absolute difference between models increase as  $f_{\text{green}}$  decreases, and  
598 as  $C_{\text{ab}}$  and  $LAI$  increase (Fig. S1n,o and S2n,o, respectively).

599



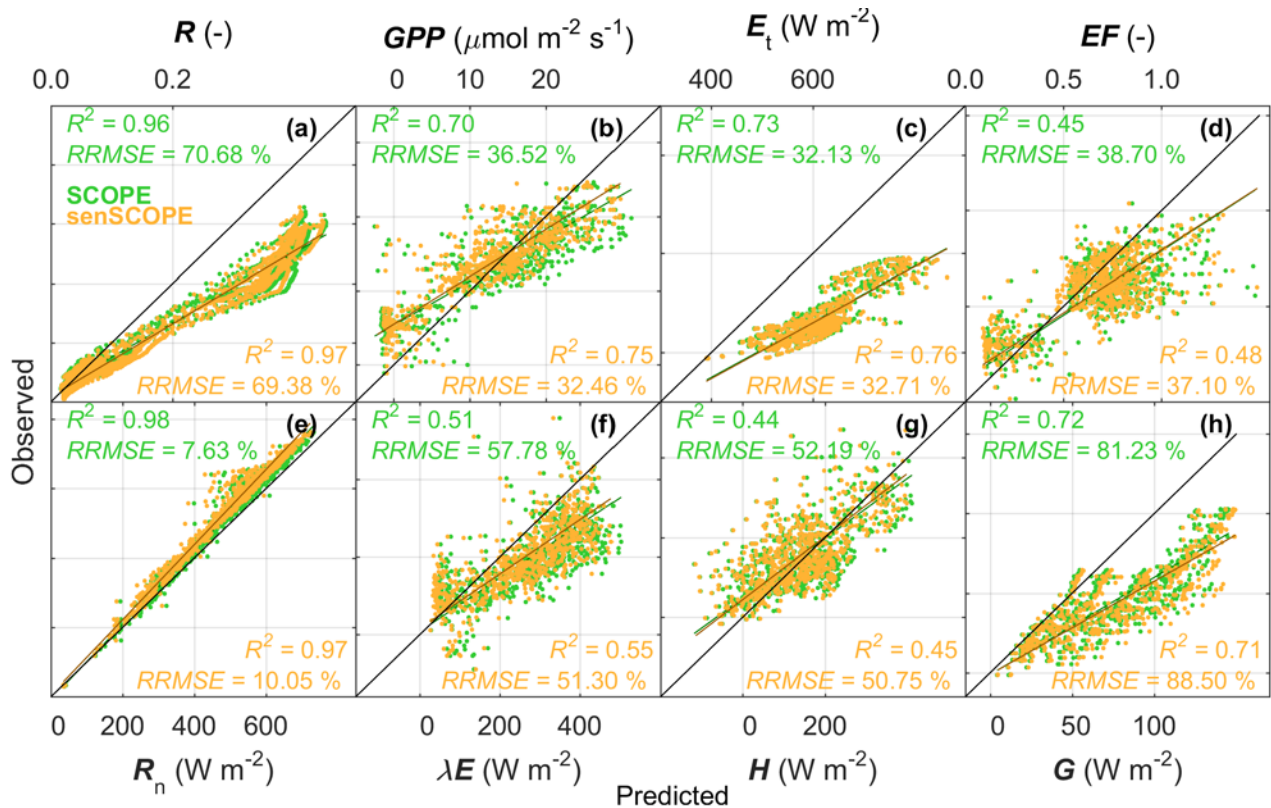


600

601 **Figure 7. Distributions of the difference between spectral variables indicative of plant physiology,**  
 602 **structure and biochemical composition simulated with SCOPE and senSCOPE in the  $F_{\text{meteo}}$  run (left**  
 603 **column) and the  $F_{\text{veg}}$  run (right column) for different fractions of green leaf area: TOC fluorescence**  
 604 **radiance at 687 nm (a,b), TOC fluorescence radiance at 760 nm (c,d), photochemical reflectance index**  
 605 **including effects of xanthophyll cycle (e,f), normalized difference vegetation index (g,h) MERIS terrestrial**  
 606 **chlorophyll index (i,j).**

## 607 4.2 Comparison with SCOPE model. Forward simulation with observational datasets

608 Fig. 8 compares the different variables predicted by SCOPE and senSCOPE vs. the fluxes measured by  
 609 the EC towers and  $R$  acquired by the airborne hyperspectral imager in the site of Majadas de Tiétar. The  
 610 comparison is done using Total Least Squares (Golub and Loan 1980). In general, senSCOPE achieves  
 611 higher coefficients of determination ( $R^2$ ) and lower relative root mean squared errors ( $RRMSE$ ). Both  
 612 models overestimate high  $R$  (Fig. 8a), and  $GPP$  (Fig. 8b); but senSCOPE is less deviated. SCOPE  
 613 overestimates  $\lambda E$  and  $EF$ , and underestimates  $H$  more than senSCOPE. Both models predict  $R_n$  quite  
 614 accurately and precisely; but senSCOPE predicts  $R_n$ ,  $E_t$  and  $G$  with slightly larger errors and in some  
 615 cases lower  $R^2$  than SCOPE.

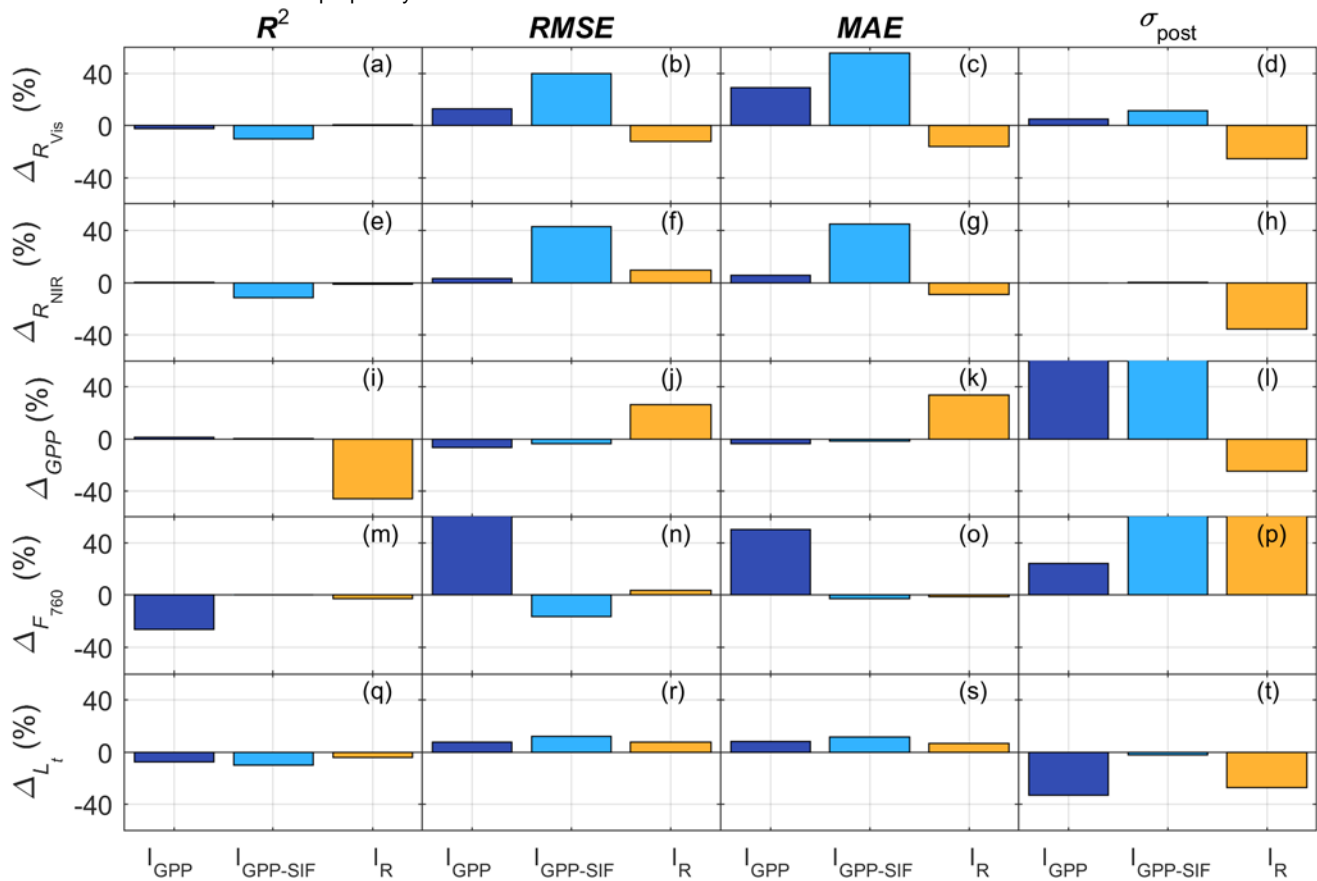


616

617 **Figure 8. Comparison of observed and predicted fluxes and reflectance factors at ecosystem scale.**  
 618 **Predictions are done by SCOPE (green) and senSCOPE (orange) using field observations or estimates of**  
 619 **vegetation properties, as well as forcing variables measured at the research station of Majadas de Tiétar**  
 620  **$\pm 1$  day around different airborne campaigns.**

### 621 **4.3 Comparison with SCOPE model. Inversion on observational datasets**

622 Fig. 9 summarizes the capability of SCOPE and senSCOPE to fit/predict the variables used as inversion  
623 constraints in the different schemes tested; notice that not all the constraints are used to optimize  
624 parameters in all the schemes. The relative differences between the statistics of the fit are calculated as  
625  $(100 \cdot (x_{\text{senSCOPE}} - x_{\text{SCOPE}}) / x_{\text{SCOPE}})$ ; where  $x$  is the statistic and the respective model is presented in the  
626 subscript.  $R^2$  is estimated using Total Least Squares (Golub and Loan 1980), and the relative root mean  
627 squared error ( $RRMSE$ ) and mean average error ( $MAE$ ) result of the comparison of the  
628 observed/predicted values. Posterior uncertainty ( $\sigma_{\text{post}}$ ) is estimated according to Omlin and Reichter  
629 (1999). The relative differences of  $R$  in the visible spectral region ( $R_{\text{vis}}$ , Fig. 9a-d) and the near infrared  
630 ( $R_{\text{NIR}}$ , Fig. 9e-h),  $GPP$  (Fig. 9i-l),  $F_{760}$  (Fig. 9m-p) and  $L_t$  (Fig. 9q-t) are presented for the three different  
631 inversion schemes tested.  $R$  is used in all the inversion schemes. senSCOPE fits  $R_{\text{vis}}$  and  $R_{\text{NIR}}$  more  
632 poorly than SCOPE in the schemes  $I_{\text{GPP}}$  and  $I_{\text{GPP-SIF}}$ ; whereas in the case of  $I_{\text{R}}$  senSCOPE these are  
633 better fit and posterior uncertainties are lower than for SCOPE. senSCOPE slightly improves the fit of  
634  $GPP$  when this is a constraint of the inversion; however,  $\sigma_{\text{post}}$  almost duplicate (values ~80%, out of the  
635 plot scale). As in Pacheco-Labrador et al., (2019)  $I_{\text{R}}$  fails to accurately fit  $GPP$ , but  $\sigma_{\text{post}}$  is lower for  
636 senSCOPE. senSCOPE fit of  $F_{760}$  improves respect to SCOPE when this is a constraint of the inversion  
637 ( $I_{\text{GPP-SIF}}$ ), but  $\sigma_{\text{post}}$  increase in all the cases. senSCOPE fits  $L_t$  more poorly than SCOPE, but  $\sigma_{\text{post}}$   
638 decrease in all the cases.

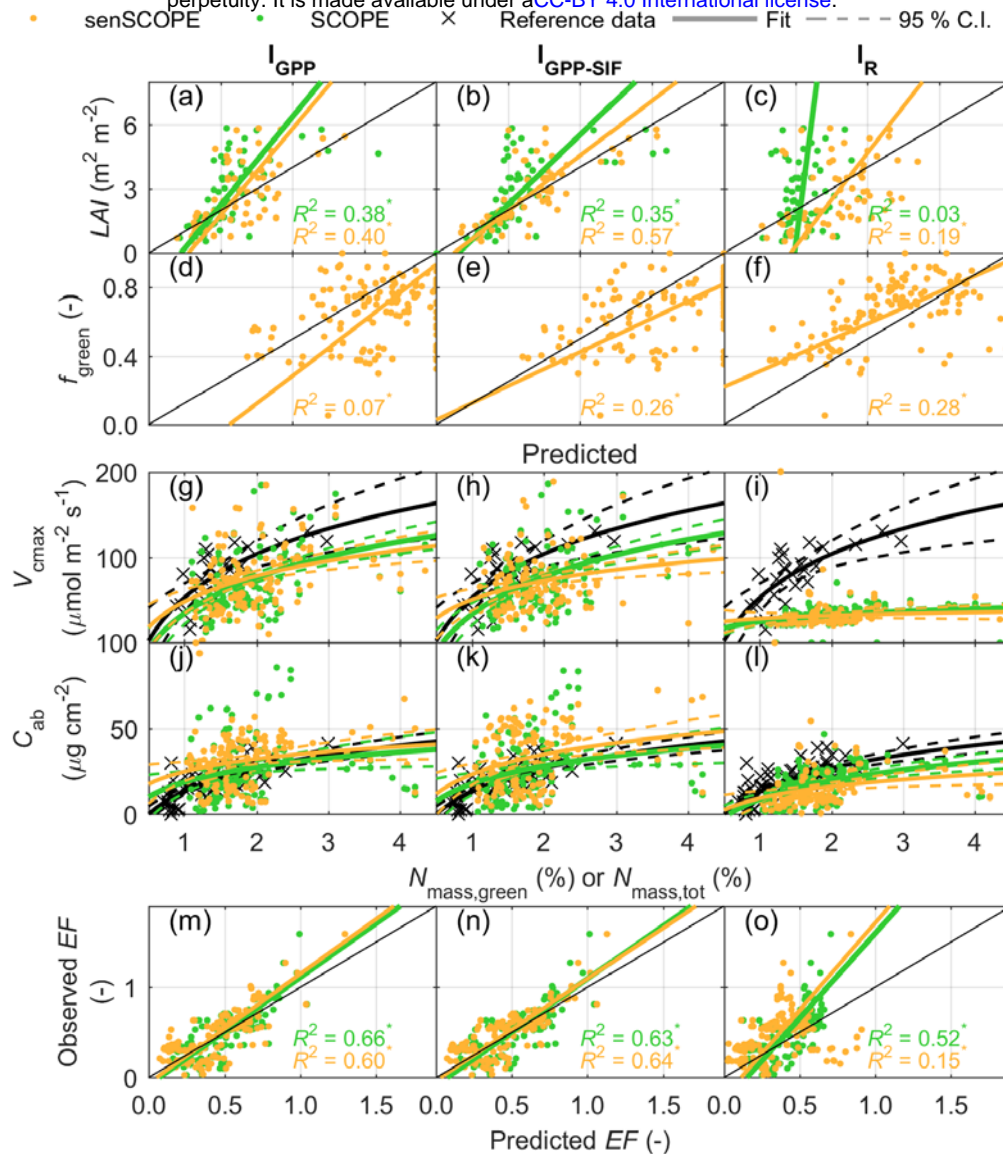


639

640 **Figure 9. Relative difference between the fit/prediction statistics of the inversion constraints obtained by**  
 641 **senSCOPE and SCOPE for the different inversion schemes.**

642 Fig. 10 compares the most relevant model parameters estimated by SCOPE and senSCOPE for the  
 643 different inversion schemes tested (presented by columns, from left to right:  $I_{\text{GPP}}$ ,  $I_{\text{GPP-SIF}}$ ,  $I_{\text{R}}$ ).  
 644 Parameters are evaluated both using field observations and pattern-oriented model evaluation approach.  
 645  $LAI$  (Fig. 10a-c) and  $f_{\text{green}}$  (Fig. 10d-f) are compared against observations using Total Least Squares  
 646 (Golub and Loan 1980). As can be seen, senSCOPE predicts similar  $LAI$  values but show higher  $R^2$  and  
 647 significance. senSCOPE is also capable of providing reasonable estimates of  $f_{\text{green}}$ , these are often  
 648 overestimated but still within the bounds of the relationship  $C_{\text{ab}} \cdot f_{\text{green}}$  observed in the site (Fig. S3).  
 649  $N_{\text{mass,green}}$  is used to evaluate  $V_{\text{cmax}}$  (Fig. 10g-i) and to compare the relationship between both variables  
 650 with the one reported in the literature for grasslands (Feng and Dietze 2013). Notice that senSCOPE

651  $V_{\text{cmax}}$  is provided per unit green leaf area and is thus comparable with SCOPE estimates and the  
652 literature data. Results are coherent with those presented in Pacheco-Labrador et al., (2019),  $I_{\text{R}}$  fails to  
653 constrain  $V_{\text{cmax}}$ , whereas the schemes using  $GPP$  provide relationships with  $N_{\text{mass,green}}$  which are closer  
654 to those in the literature.  $V_{\text{cmax}}$  estimates are very similar for both models in  $I_{\text{GPP}}$ ; however, the use of  
655  $F_{760}$  in  $I_{\text{GPP-SIF}}$  seems to slightly deviate the adjusted logarithmic model from the one fit to the data in  
656 Feng and Dietze (2013). Similarly,  $C_{\text{ab}}$  (per total leaf area) is evaluated against  $N_{\text{mass}}$  of the whole  
657 canopy (Fig. 10j-l), and their relationship is compared with field observations of both variables in the  
658 site of Majadas de Tiétar. When  $GPP$  constrains the inversion senSCOPE and SCOPE estimates are  
659 similar and follow the relationship observed in the field. However, as in Pacheco-Labrador et al.,  
660 (2019), SCOPE  $I_{\text{GPP}}$  and  $I_{\text{GPP-SIF}}$  estimates present high values during the dry period, which stand out of  
661 the relationship with  $N_{\text{mass}}$  between 0.5-1.3 %. senSCOPE corrects most of these values, especially in  
662 the scheme  $I_{\text{GPP}}$ ; while the scheme  $I_{\text{GPP-SIF}}$  still preserves some of these high values. Fig. 10m-o  
663 compares predicted and observed  $EF$  using Total Least Squares (Golub and Loan 1980). In general,  
664 both models achieve similar results when  $GPP$  constrains the inversion; however, senSCOPE  $R^2$  are  
665 lower than in SCOPE. As in Pacheco-Labrador et al., (2019),  $I_{\text{R}}$  fails to constrain functional parameters.



666

667 **Figure 10. Summary of the parameters' evaluation using observations and pattern-oriented model**  
 668 **evaluation for the four inversion schemes tested. Leaf area index, (a-c) and green fraction of leaf surface**  
 669 **(d-f), and evaporative fraction (q-t) are compared with field observation using Total Least Squares (Golub**  
 670 **and Loan 1980). Significance is described with the symbols <sup>•</sup> for  $p$ -values  $0.05 \leq p < 0.10$ ; and <sup>\*</sup> for  $p < 0.05$ .**  
 671 **The 1:1 line is shown in black. Maximum carboxylation rate (g-i) and chlorophyll concentration (j-p) are**  
 672 **evaluated against nitrogen content in green leaves and total nitrogen content, respectively and compared**  
 673 **with data from the literature (Feng and Dietze 2013) the first, and relationships observed in the field, the**  
 674 **second A logarithmic relationship is fit in both cases, the 95 % confidence interval is show with dashed**  
 675 **lines.**



## 676 5. Discussion

677 This manuscript describes and evaluates senSCOPE, a version of the model SCOPE representing  
678 separately radiative transfer and physiological processes of green and senescent leaves; which is  
679 relevant in canopies featuring important senescent leaf area fractions. senSCOPE is evaluated against  
680 SCOPE 1) by direct comparison of forward synthetic simulations, 2) by comparison of simulated and  
681 observed ecosystem-scale fluxes and reflectance factors, and 3) by evaluation of parameter estimates  
682 and predicted variables via inversion of the models against a comprehensive dataset including  
683 hyperspectral optical  $R$ , as well as  $GPP$ , SIF and TIR radiance. These data were collected in a  
684 fertilization experiment with varying nitrogen and phosphorous additions and degrees of water stress.  
685 Results show that in senescent canopies senSCOPE improves the forward modelling of radiative  
686 transfer, photosynthesis and fluxes; and that in inversion -if suitably constrained-, it improves the  
687 estimation of  $C_{ab}$ . At the same time, the performance of both models is comparable when green leaves  
688 dominate.

689 senSCOPE distributes senescent and remaining pigments in two conceptual leaves (green and  
690 senescent) and predicts separately their respective optical properties, which are later combined. This  
691 approach was already proposed by Bach et al., (2001) and used in later works (Bach and Verhoef 2003;  
692 Houborg et al. 2009; Houborg et al. 2015; Houborg and McCabe 2016; Verhoef and Bach 2003). This  
693 dual-leaf approach generates averaged “brighter” leaves since not all the absorbent species are located  
694 in the same leaf (Fig. 3). This has relevant consequences for the canopy-RTM, especially in those  
695 spectral regions where senescent and the rest of the pigments overlap, and therefore for  $APAR_{Chl}$ .  
696 senSCOPE produces reflectance factors and  $APAR_{Chl}$  that close-to-linearly vary with  $f_{green}$ ; whereas in  
697 the case of SCOPE, these variables vary logarithmically with  $f_{green}$  since leaves absorptivity saturate due  
698 to the large presence of pigments. This saturation, combined with the fact that  $R_{NIR}$  was overestimated  
699 during senescence, led to unrealistically high  $C_{ab}$  estimates during the dry period when a strong  
700 functional constraint  $-GPP-$  was used (Pacheco-Labrador et al. 2019). Notice that only the constraint  
701  $GPP$  provided robust estimates of functional parameters. In the present work, we repeated the inversion  
702 of SCOPE allowing higher  $C_s$  than in Pacheco-Labrador (2019) since this allowed predicting low  $R_{NIR}$



703 values observed in the site (Martín et al. 2019). This approach improved the fit of  $R_{\text{NIR}}$  for all inversion  
704 schemes during SCOPE inversion (not shown), but did not solve the overestimation of  $C_{\text{ab}}$  in the most  
705 strongly constrained schemes ( $I_{\text{GPP}}$  and  $I_{\text{GPP-SIF}}$ , Fig. 10a,b). senSCOPE fitted less precisely the  
706 inversion constraints, and in some cases posterior uncertainties increased due to the strong control that  
707  $f_{\text{green}}$  has on most of the model outputs (Fig. 9). For  $I_{\text{R}}$  senSCOPE improved the fit of  $R$ , but the opposite  
708 occurred when  $a\text{PAR}$  was constrained by  $\text{GPP}$ , suggesting that the model might not still represent  
709 accurately the observed grassland. However, senSCOPE led to  $C_{\text{ab}}$  values more soundly related with  
710  $N_{\text{mass}}$  than SCOPE during the dry season (schemes  $I_{\text{GPP}}$  and  $I_{\text{GPP-SIF}}$ , Fig. 10j,k).

711 The fact that senSCOPE limits photosynthesis and transpiration to the green fraction results in a close-  
712 to-linear relation between  $f_{\text{green}}$  on the one hand, and  $A$  and  $\lambda E$  on the other hand (Fig. 4 and 5). SCOPE  
713 predicts higher assimilation and transpiration unless  $f_{\text{green}}$  is very low ( $\sim 0$ ); in that case  $A$  is negative  
714 while  $\lambda E$  is still high. Contrarily,  $R_{\text{n}}$  and  $G$  predictions are similar for both models; also, differences in  $H$   
715 are lower than for  $\lambda E$ , but still in senSCOPE  $H$  varies more linearly with  $f_{\text{green}}$  than in SCOPE (notice  
716 that  $f_{\text{green}}$  is not a SCOPE parameter, but is used to average leaf parameters). In the forward simulation at  
717 ecosystem scale senSCOPE predicted most of the ecosystem fluxes better than SCOPE (Fig. 8). In this  
718 case we assumed a fixed value for  $m$ , which might be not completely realistic; however additional  
719 works at ecosystem scale have shown that senSCOPE can more robustly represent water use efficiency  
720 than SCOPE (not shown). In the inversion at plot level, senSCOPE predicted  $\text{GPP}$  better than SCOPE  
721 when used as constraint (Fig. 9k-o). In contrast,  $EF$  was predicted more poorly in all the schemes.  
722 senSCOPE assumes no transpiration from senescent leaves; however evaporation from their surface  
723 might be relevant when these are moisturized by dew or rainfall. Neither SCOPE nor senSCOPE  
724 represent that process and their use after such situations might result uncertain.

725 In inversion, both SCOPE and senSCOPE underestimated  $LAI$ , while senSCOPE overestimated  $f_{\text{green}}$   
726 (Fig. 10a-h). As discussed in Pacheco-Labrador et al, (2019) and Melendo-Vega (2018), the optical  
727 properties of dry standing material might not be accurately described by RTM, leading to an  
728 overestimation of  $R_{\text{NIR}}$ , which seems to be counter-weighted in inversion by reducing  $LAI$ . In fact,  
729 inversion schemes using  $\text{GPP}$  ( $I_{\text{GPP}}$  and  $I_{\text{GPP-SIF}}$ ) improved the estimation of  $LAI$  since  $\text{GPP}$  demands

730 higher  $APAR_{Chl}$  in exchange for increasing the fitting error of  $R_{NIR}$  (Pacheco-Labrador et al., (2019), this  
731 work). In senSCOPE, underestimation of  $LAI$  was also compensated also by overestimating  $f_{green}$ . These  
732 facts suggest that the optical properties of the senescent material and/or the death standing material of  
733 this grassland (and likely other ecosystems) are not accurately represented, leading to biased estimates  
734 of some of the parameters. In fact, it was necessary increasing the upper bound of  $C_s$  to be able to  
735 predict low  $R_{NIR}$  in the dry season. We allowed  $C_s$  up to 7.5; whereas values up to 5.0 are reported in  
736 literature (Houborg and Anderson 2009). Too high  $C_s$  might have led to unrealistic representation of  $\rho$   
737 and  $\tau$  of senescent leaves, very dark in the visible region but also with low  $R_{NIR}$ . In some cases SCOPE  
738 estimated  $C_s = 7.5$ , whereas senSCOPE predicted  $C_s < 5$  in most of the cases (Fig. S4c). Apart from  
739  $LAI$ ,  $C_{dm}$  and  $C_w$ , -which are weakly constrained because the spectroradiometric measurements did not  
740 include the short wave infrared range (SWIR)-, might have been affected by this problem. SCOPE and  
741 senSCOPE estimates of  $C_{dm}$  often hit the upper bound established from observations in the field. High  
742  $C_{dm}$  also serves to reduce  $R_{NIR}$ . In contrast, senSCOPE  $C_w$  estimates are less often saturated;  $C_w$  has  
743 little effect below 970 nm, but influences leaf optical properties in the SWIR. The relationship between  
744  $N$ ,  $C_{dm}$  and  $C_w$  of green and senescent leaves assumed during inversion might have contributed to  
745 increase the uncertainty of the parameter estimates; for example, it has been observed that leaf thickness  
746 decreases during senescence (Castro and Sanchez-Azofeifa 2008); whereas other works assign high  $N$   
747 values to senescent leaves (Houborg et al. 2009). However, a balance between model error and  
748 equifinality must be also observed. Site-specific relationships between the parameters of each leaf type  
749 or relationships found in global databases could be used in the future to improve the representation of  
750 semi-arid canopies. senSCOPE does not include improved calibrated absorption coefficients or  
751 refractive indices to more realistically represent senescent leaves and death standing material, but it  
752 offers a formally more correct representation of mixed canopies. The model improves the representation  
753 of these canopies, which could be used in the future to calibrate or validate specific absorption spectra  
754 of senescent material. senSCOPE can also be applied to other canopies, such as crops and forests, which  
755 are characterized a senescent stage. Moreover, the approach adopted in senSCOPE could be similarly  
756 used to represent other mixed canopies combining plants with different biophysical properties and  
757 function, such as C3 and C4 species. An additional problem for the representation of mixed canopies

758 would be the vertical distribution of the senescent material. The impact on the observed  $R$  and fluxes is  
759 unclear, and further research is needed in this direction. In such studies, senSCOPE could also be  
760 extended to other versions of SCOPE, such as mSCOPE (Yang et al. 2017) to describe the vertical  
761 distribution of senescent matter.

762  $f_{\text{green}}$  is a critical parameter in senSCOPE, it strongly controls RTM and fluxes and increases equifinality  
763 of the inverse problem. Thus, the use of prior information about this variable is strongly  
764 recommended during inversion. For this reason, in this work  $f_{\text{green}}$  was indirectly predicted from leaf  
765 parameter estimates using a NN while the model was inverted. The design of this model was critical to  
766 achieve acceptable results, and during training  $C_{\text{ab}}$  (and  $C_{\text{ca}}$ ) had to be limited to the ranges observed in  
767 the study site (up to  $\sim 40 \mu\text{g cm}^{-2}$ ). During inversion higher  $C_{\text{ab}}$  values were allowed, but still,  $C_{\text{ab}} \cdot f_{\text{green}}$   
768 estimates stood within or very close to the bounds observed and used to train the NN (Fig. S3)

769 As a result of the combination of changes in RTM and photosynthesis, not only carbon and water  
770 fluxes, but also photosynthetic efficiency and downregulation resulted modified (Fig. 6). On one side,  
771 senSCOPE tends to predict higher canopy temperatures than SCOPE, especially when  $f_{\text{green}}$  decreases.  
772 Senescent leaves are warmer than green leaves, but senSCOPE green leaves are not necessarily cooler  
773 than SCOPE leaves (not shown). Leaf temperature strongly influences photosynthetic efficiency and  
774 together with  $APAR_{\text{Chl}}$  on photosynthesis down-regulation. Fig. 4m,h show how senSCOPE diel cycles  
775 of  $K_n$  reach higher midday values than SCOPE. SCOPE predicts larger variability of  $K_n$  as a function of  
776  $f_{\text{green}}$  under conditions of low illumination, whereas senSCOPE  $K_n$  varies more strongly with  $f_{\text{green}}$  under  
777 high temperature and irradiance conditions (not shown). Non-photochemical quenching has also  
778 different effects on the predicted  $\Phi'_f$ . For example, Fig. 4o,p show how senSCOPE predicts a decrease  
779 of this efficiency at midday whereas this is hardly noticeable for SCOPE.  $K_n$  and  $\Phi'_f$  are fundamental  
780 variables to mechanistically interpret SIF signals to determine functional status of vegetation and stress  
781 (Frankenberg and Berry 2018; Porcar-Castell et al. 2014). Thus considering the differences shown, both  
782 models can lead to very different interpretations. Adequate representation of physiological processes  
783 and their drivers is fundamental to mechanistically interpret these signals; but also the representation of  
784 the spectral variables used to obtain information about these processes, such as fluorescence radiance or

785 *PRI*. Similarly as *R*, spectral indices vary more linearly with  $f_{\text{green}}$  in senSCOPE than in SCOPE (e.g.,  
786 Fig. 4q,r). Unlike other spectroradiometric variables, *PRI* show no clear differences between models  
787 (e.g. distributions of the difference centre around 0). *PRI* is known to result sensitive to pigments pool,  
788 ratio and to *LAI* (Gamon and Berry 2012; Garbulsy et al. 2011); results of this work also show that this  
789 index is also strongly sensitive to the presence of senescent material. The magnitude of SIF emissions is  
790 also modified by senSCOPE, which tends to predict less SIF when  $f_{\text{green}}$  decreases, (Fig. 7a-d).

791 In this study we compare the inversion of SCOPE and senSCOPE using the data and approaches of in  
792 Pacheco-Labrador et al, (2019), but allowing for higher values for  $C_s$  (as well as  $C_{\text{dm}}$  and  $C_w$ ). The  
793 wider parameter bounds did not change significantly the results obtained with SCOPE, and differences  
794 were mainly related to the use of senSCOPE; which improved the estimation of  $C_{\text{ab}}$  in the dry season.  
795 As with SCOPE, SIF (not shown) and *R* failed to constrain functional parameters (e.g.,  $V_{\text{cmax}}$ ) and *LAI*;  
796 and only inversion schemes relying on *GPP* provided robust estimates. However with senSCOPE, the  
797 schemes relying on SIF reduced their performance respect to SCOPE.  $I_{\text{GPP-SIF}}$  fitted the inversion  
798 constraints more poorly, and could not correct high  $C_{\text{ab}}$  estimates during senescence as much as  $I_{\text{GPP}}$ .  
799 This might be result from the use of large  $C_s$ , which suggests further work is needed to more accurately  
800 characterize the optical properties of death standing and senescent material. Also for senSCOPE,  
801 functional parameters resulted insensitive to  $I_R$  constraints (partly due to inversion method, see  
802 Pacheco-Labrador et al, (2019)). Bayat et al., (2018) inverted SCOPE using *R* and found troubles to  
803 predict low *GPP* and  $\lambda E$  in a grassland during senescence, which was corrected constraining the model  
804 with *R* and TIR radiance to reduce  $V_{\text{cmax}}$  during this period. Fig. 10i-l compares  $V_{\text{cmax}}$  estimates of both  
805 models; for senSCOPE  $V_{\text{cmax}}$  is presented respect to green leaf area, whereas in SCOPE, it is presented  
806 respect to total leaf area (all considered “green”). As can be seen, when adequately constrained  
807 estimates of both models are comparable. In senSCOPE *GPP* scales with  $f_{\text{green}}$ , and  $V_{\text{cmax}}$  (in the green  
808 leaves) does not need to decrease to predict low assimilation.

809 senSCOPE is computationally more demanding (around 10% slower) than SCOPE since more  
810 processes and calculations are needed, and more iterations are required to close the energy balance  
811 (Table S5). However, senSCOPE seems more robust and provides lower energy balance closure error.

812 Since performance of both models is similar for large  $f_{\text{green}}$ , both models can be alternately used through  
813 the season according the presence of senescent material.

## 814 **6. Conclusions**

815 The combination of advanced radiative transfer models with models representing exchanges of matter  
816 and energy between vegetation, soil and atmosphere is bringing new opportunities to improve our  
817 understanding of ecosystem function from remote observations. For example, the model SCOPE is  
818 being used in the last years with this purpose. However, the accuracy with which these models represent  
819 reality limits their application; and ecosystem-specific features can bias results and their interpretation.  
820 In this context, we present the model senSCOPE; which adapts SCOPE radiative transfer, energy  
821 balance, photosynthesis and transpiration in homogeneous canopies with mixed green and dry leaves.  
822 The separated representation of green and senescent leaves significantly modifies the simulation of  
823 fluxes and spectra signals respect to a model featuring a single leaf with “averaged” properties.  
824 senSCOPE reflectance factors, carbon assimilation and water and energy fluxes linearly scale with  $f_{\text{green}}$ ;  
825 it also improves the prediction of these variables in forward simulations as well as the estimation of  
826 vegetation parameters, notably  $C_{\text{ab}}$ , during the dry season. This is significant for the remote sensing of  
827 vegetation function of semi-arid ecosystems, and potentially for phenology monitoring. Despite the  
828 improvements, results suggest that not only model structure needs to be corrected; a more accurate  
829 characterization of the optical properties of senescent material in grasslands is still needed. The use of  
830 SCOPE and derived models is growing in the remote sensing community; however, further assessment  
831 of their performance to inform about plant function should be tested in different ecosystems. For  
832 example, the role of vertical and horizontal heterogeneity is still unclear. Robust evaluation, e.g.  
833 pattern-oriented model evaluation approach, would contribute to identify caveats and ecosystem-  
834 specific features that prevent accurate monitoring of their function; and that therefore, should be also  
835 represented.

## 836 **Appendix A: Green fraction Neural Network predictor**

837 In senSCOPE inversion, the fraction of green leaf area in the canopy ( $f_{\text{green}}$ ) is estimated as a function of  
838 the canopy averaged leaf RTM parameters using a NN model trained from simulated data. Latin  
839 Hypercube Sampling was used to generate a look-up table (LUT) with 5000 samples of different leaf  
840 constituents ( $C_{\text{ab}}$ ,  $C_{\text{ant}}$ ,  $C_{\text{dm}}$ ,  $C_{\text{w}}$ ,  $C_{\text{s}}$ ),  $N$  and  $f_{\text{green}}$ .  $C_{\text{ca}}$  was included in the LUT as a function of  $C_{\text{ab}}$   
841 according to the relationship reported in Sims and Gamon (2002), and an uncertainty estimated in the  
842 relationship of  $\sim 4.5 \mu\text{g cm}^{-2}$  according to field measurements was used to add Gaussian noise. The same  
843 bounds that were applied in inversion (Section 3.3.2) were used to design the LUTs; however  $C_{\text{ab}}$  and  
844  $C_{\text{ca}}$  of green leaves were limited to 40 and  $10 \mu\text{g cm}^{-2}$ , respectively; according to field observations.  
845 LUT values were assumed to belong to pure green and senescent leaves, and averaged leaf parameters  
846 were mixed according with Eq. 21, assuming that in green leaves  $C_{\text{s}} = 0$ , and that in senescent leaves  
847  $C_{\text{ab}} = 0$ ,  $C_{\text{ca}} = 0$ ,  $C_{\text{ant}} = 0$ . No additional assumptions about the values of the parameters of each leaf type  
848 and therefore the  $N$ ,  $C_{\text{dm}}$ ,  $C_{\text{w}}$  were taken directly from the LUT.

849 A NN was trained using SimpleR (Camps-Valls et al. 2012) to predict  $f_{\text{green}}$  as function of the canopy  
850 averaged leaf RTM parameters. During the training, 60 % of the dataset was used for fitting and 40 %  
851 for testing. Performance statistics are presented in Table A1.

852 Table A1. Statistics of the fraction green leaf area ( $f_{\text{green}}$ ) Neural Network (NN) model.

Dataset	$R^2$	RMSE	ME	MAE
Training	0.818	0.123	0.005	0.093
Validation	0.718	0.230	0.158	0.180

## 853 **Author contributions**

854 JPL, TSEM, MM and CvdT designed the model. JPL and MM designed model evaluation. TSEM, AC,  
855 OPP, JG, PM, RGC, GM, MR and MM provided measurements of fluxes, plant parameters and spectral  
856 variables. JPL, CvdT, MM, OPP, JG, PM and RGC wrote the paper.



## 857 **Acknowledgements**

858 JPL, MM and MR acknowledge the EnMAP project MoReDEHESHyReS “Modelling Responses of  
859 Dehesas with Hyperspectral Remote Sensing” (Contract No. 50EE1621, German Aerospace Center  
860 (DLR) and the German Federal Ministry of Economic Affairs and Energy). Authors acknowledge the  
861 Alexander von Humboldt Foundation for supporting this research with the Max-Planck Prize to Markus  
862 Reichstein; the project SynerTGE “Landsat-8+Sentinel-2: exploring sensor synergies for monitoring  
863 and modelling key vegetation biophysical variables in tree-grass ecosystems” (CGL2015-69095-R,  
864 MINECO/FEDER,UE); and the project FLUXPEC “Monitoring changes in water and carbon fluxes  
865 from remote and proximal sensing in Mediterranean ‘dehesa’ ecosystem” (CGL2012-34383, Spanish  
866 Ministry of Economy and Competitiveness). Authors are very thankful to the MPI-BGC Freiland Group  
867 and especially Olaf Kolle, Martin Hertel as well as Ramón López-Jiménez (CEAM) for technical  
868 assistance. We are grateful to all the colleagues from MPI-BGC, University of Extremadura, University  
869 of Milano-Bicocca, SpecLab-CSIC, INIA and CEAM which have collaborated in any of the field and  
870 laboratory works. We acknowledge the Majadas de Tiétar city council for its support.

## 871 **References**

- 872 Anderson, R.C. (2006). Evolution and origin of the Central Grassland of North America: climate, fire,  
873 and mammalian grazers. *The Journal of the Torrey Botanical Society*, 133, 626-647, 622
- 874 Bach, H., Schneider, K., Verhoef, W., Stolz, R., Mauser, W., Van Leeuwen, H., Schouten, L., &  
875 Borgeaud, M. (2001). *Retrieval of geo-and biophysical information from remote sensing through*  
876 *advanced combination of a land surface process model with inversion techniques in the optical and*  
877 *microwave spectral range.*
- 878 Bach, H., & Verhoef, W. (2003). Sensitivity studies on the effect of surface soil moisture on canopy  
879 reflectance using the radiative transfer model GeoSAIL. In, *IGARSS 2003. 2003 IEEE International*  
880 *Geoscience and Remote Sensing Symposium. Proceedings (IEEE Cat. No.03CH37477)* (pp. 1679-1681)
- 881 Bacour, C., Jacquemoud, S., Leroy, M., Hauteceur, O., Weiss, M., Prévot, L., Bruguier, N., & Chauki,  
882 H. (2002). Reliability of the estimation of vegetation characteristics by inversion of three canopy  
883 reflectance models on airborne POLDER data. *Agronomie*, 22, 555-565



- 884 Bayat, B., van der Tol, C., & Verhoef, W. (2018). Integrating satellite optical and thermal infrared  
885 observations for improving daily ecosystem functioning estimations during a drought episode. *Remote*  
886 *Sensing of Environment*, 209, 375-394
- 887 Braswell, B.H., Schimel, D.S., Privette, J.L., Moore Iii, B., Emery, W.J., Sulzman, E.W., & Hudak,  
888 A.T. (1996). Extracting ecological and biophysical information from AVHRR optical data: An  
889 integrated algorithm based on inverse modeling. *Journal of Geophysical Research: Atmospheres*, 101,  
890 23335-23348
- 891 Camino, C., Gonzalez-Dugo, V., Hernandez, P., & Zarco-Tejada, P.J. (2019). Radiative transfer Vcmax  
892 estimation from hyperspectral imagery and SIF retrievals to assess photosynthetic performance in  
893 rainfed and irrigated plant phenotyping trials. *Remote Sensing of Environment*, 111186
- 894 Camps-Valls, G., Munoz-Mari, J., Gomez-Chova, L., Guanter, L., & Calbet, X. (2012). Nonlinear  
895 Statistical Retrieval of Atmospheric Profiles From MetOp-IASI and MTG-IRS Infrared Sounding Data.  
896 *IEEE Transactions on Geoscience and Remote Sensing*, 50, 1759-1769
- 897 Castro, K.L., & Sanchez-Azofeifa, G.A. (2008). Changes in Spectral Properties, Chlorophyll Content  
898 and Internal Mesophyll Structure of Senescing Populus balsamifera and Populus tremuloides Leaves.  
899 *Sensors (Basel, Switzerland)*, 8, 51-69
- 900 Cleland, E.E., Chiariello, N.R., Loarie, S.R., Mooney, H.A., & Field, C.B. (2006). Diverse responses of  
901 phenology to global changes in a grassland ecosystem. *Proceedings of the National Academy of*  
902 *Sciences*, 103, 13740
- 903 Croft, H., Chen, J.M., Luo, X., Bartlett, P., Chen, B., & Staebler, R.M. (2017). Leaf chlorophyll content  
904 as a proxy for leaf photosynthetic capacity. *Global Change Biology*, 23, 3513-3524
- 905 Dash, J., & Curran, P.J. (2007). Evaluation of the MERIS terrestrial chlorophyll index (MTCI).  
906 *Advances in Space Research*, 39, 100-104
- 907 Dutta, D., Schimel, D.S., Sun, Y., van der Tol, C., & Frankenberg, C. (2019). Optimal inverse  
908 estimation of ecosystem parameters from observations of carbon and energy fluxes. *Biogeosciences*, 16,  
909 77-103
- 910 El-Madany, T.S., Reichstein, M., Perez-Priego, O., Carrara, A., Moreno, G., Pilar Martín, M., Pacheco-  
911 Labrador, J., Wohlfahrt, G., Nieto, H., Weber, U., Kolle, O., Luo, Y.-P., Carvalhais, N., & Migliavacca,  
912 M. (2018). Drivers of spatio-temporal variability of carbon dioxide and energy fluxes in a  
913 Mediterranean savanna ecosystem. *Agricultural and Forest Meteorology*, 262, 258-278
- 914 Feng, X., & Dietze, M. (2013). Scale dependence in the effects of leaf ecophysiological traits on  
915 photosynthesis: Bayesian parameterization of photosynthesis models. *New Phytologist*, 200, 1132-1144
- 916 Feret, J.-B., François, C., Asner, G.P., Gitelson, A.A., Martin, R.E., Bidel, L.P.R., Ustin, S.L., le Maire,  
917 G., & Jacquemoud, S. (2008). PROSPECT-4 and 5: Advances in the leaf optical properties model  
918 separating photosynthetic pigments. *Remote Sensing of Environment*, 112, 3030-3043

- 919 Féret, J.B. (2009). Apport de la modélisation pour l'estimation de la teneur en pigments foliaires par  
920 télédétection. In (p. 214): Université Pierre et Marie Curie
- 921 Féret, J.B., Gitelson, A.A., Noble, S.D., & Jacquemoud, S. (2017). PROSPECT-D: Towards modeling  
922 leaf optical properties through a complete lifecycle. *Remote Sensing of Environment*, *193*, 204-215
- 923 Figueroa, M.E., & Davy, A.J. (1991). Response of Mediterranean Grassland Species to Changing  
924 Rainfall. *Journal of Ecology*, *79*, 925-941
- 925 Frankenberg, C., & Berry, J. (2018). 3.10 - Solar Induced Chlorophyll Fluorescence: Origins, Relation  
926 to Photosynthesis and Retrieval A2 - Liang, Shunlin. *Comprehensive Remote Sensing* (pp. 143-162).  
927 Oxford: Elsevier
- 928 Friedlingstein, P., Meinshausen, M., Arora, V.K., Jones, C.D., Anav, A., Liddicoat, S.K., & Knutti, R.  
929 (2014). Uncertainties in CMIP5 Climate Projections due to Carbon Cycle Feedbacks. *Journal of*  
930 *Climate*, *27*, 511-526
- 931 Gamon, J.A., & Berry, J.A. (2012). Facultative and constitutive pigment effects on the Photochemical  
932 Reflectance Index (PRI) in sun and shade conifer needles. *Israel Journal of Plant Sciences*, *60*, 85-95
- 933 Gamon, J.A., Peñuelas, J., & Field, C.B. (1992). A narrow-waveband spectral index that tracks diurnal  
934 changes in photosynthetic efficiency. *Remote Sensing of Environment*, *41*, 35-44
- 935 Garbulsky, M.F., Peñuelas, J., Gamon, J., Inoue, Y., & Filella, I. (2011). The photochemical reflectance  
936 index (PRI) and the remote sensing of leaf, canopy and ecosystem radiation use efficiencies: A review  
937 and meta-analysis. *Remote Sensing of Environment*, *115*, 281-297
- 938 Golub, G.H., & Loan, C.F.v. (1980). An Analysis of the Total Least Squares Problem. *SIAM Journal on*  
939 *Numerical Analysis*, *17*, 883-893
- 940 Gonzalez-Cascon, R., Jiménez-Fenoy, L., Verdú-Fillola, I., & Martín, M.P. (2017). Short  
941 communication: Aqueous-acetone extraction improves the drawbacks of using dimethylsulfoxide as  
942 solvent for photometric pigment quantification in *Quercus ilex* leaves. *2017*, *26*
- 943 Gonzalez-Cascon, R., & Martin, M.P. (2018). Protocol for pigment content quantification in herbaceous  
944 covers: sampling and analysis, *October 2019*
- 945 Guyot, S., Vercauteren, J., & Cheynier, V. (1996). Structural determination of colourless and yellow  
946 dimers resulting from (+)-catechin coupling catalysed by grape polyphenoloxidase. *Phytochemistry*, *42*,  
947 1279-1288
- 948 He, Y., & Mui, A. (2010). Scaling up Semi-Arid Grassland Biochemical Content from the Leaf to the  
949 Canopy Level: Challenges and Opportunities. *Sensors*, *10*, 11072-11087
- 950 Henry, H.A.L., Brizgys, K., & Field, C.B. (2008). Litter Decomposition in a California Annual  
951 Grassland: Interactions Between Photodegradation and Litter Layer Thickness. *Ecosystems*, *11*, 545-554
- 952 Hörtensteiner, S. (2006). CHLOROPHYLL DEGRADATION DURING SENESCENCE. *Annual*  
953 *Review of Plant Biology*, *57*, 55-77

- 954 Houborg, R., & Anderson, M. (2009). Utility of an image-based canopy reflectance modeling tool for  
955 remote estimation of LAI and leaf chlorophyll content at regional scales. In (p. 29): SPIE
- 956 Houborg, R., Anderson, M., & Daughtry, C. (2009). Utility of an image-based canopy reflectance  
957 modeling tool for remote estimation of LAI and leaf chlorophyll content at the field scale. *Remote*  
958 *Sensing of Environment*, 113, 259-274
- 959 Houborg, R., & Boegh, E. (2008). Mapping leaf chlorophyll and leaf area index using inverse and  
960 forward canopy reflectance modeling and SPOT reflectance data. *Remote Sensing of Environment*, 112,  
961 186-202
- 962 Houborg, R., McCabe, M., Cescatti, A., Gao, F., Schull, M., & Gitelson, A. (2015). Joint leaf  
963 chlorophyll content and leaf area index retrieval from Landsat data using a regularized model inversion  
964 system (REGFLEC). *Remote Sensing of Environment*, 159, 203-221
- 965 Houborg, R., & McCabe, M.F. (2016). Adapting a regularized canopy reflectance model (REGFLEC)  
966 for the retrieval challenges of dryland agricultural systems. *Remote Sensing of Environment*, 186, 105-  
967 120
- 968 IPCC (2014). Climate Change 2014: Synthesis Report. Contribution of Working Groups I, II and III to  
969 the Fifth Assessment Report of the Intergovernmental Panel on Climate Change. In R.K.P.a.L.A. Meyer  
970 (Ed.) (p. 151). Geneva, Switzerland: IPCC
- 971 Jacquemoud, S. (1988). Modélisation des propriétés optiques des feuilles. In: USTL / ENSA  
972 Montpellier / INRA
- 973 Jacquemoud, S., & Baret, F. (1990). PROSPECT: A model of leaf optical properties spectra. *Remote*  
974 *Sensing of Environment*, 34, 75-91
- 975 Jacquemoud, S., Verhoef, W., Baret, F., Bacour, C., Zarco-Tejada, P.J., Asner, G.P., François, C., &  
976 Ustin, S.L. (2009). PROSPECT+SAIL models: A review of use for vegetation characterization. *Remote*  
977 *Sensing of Environment*, 113, S56-S66
- 978 Kidnie, S., Cruz, M.G., Gould, J., Nichols, D., Anderson, W., & Bessell, R. (2015). Effects of curing on  
979 grassfires: I. Fuel dynamics in a senescing grassland. *International Journal of Wildland Fire*, 24, 828-  
980 837
- 981 Koukoura, Z., Mamolos, A.P., & Kalburtji, K.L. (2003). Decomposition of dominant plant species litter  
982 in a semi-arid grassland. *Applied Soil Ecology*, 23, 13-23
- 983 Luo, Y., El-Madany, T., Filippa, G., Ma, X., Ahrens, B., Carrara, A., Gonzalez-Cascon, R., Cremonese,  
984 E., Galvagno, M., Hammer, T., Pacheco-Labrador, J., Martín, M., Moreno, G., Perez-Priego, O.,  
985 Reichstein, M., Richardson, A., Römermann, C., & Migliavacca, M. (2018). Using Near-Infrared-  
986 Enabled Digital Repeat Photography to Track Structural and Physiological Phenology in Mediterranean  
987 Tree-Grass Ecosystems. *Remote Sensing*, 10, 1293
- 988 Martín, M.P., Pacheco-Labrador, J., Gonzalez-Cascon, R., Moreno, G., Migliavacca, M., García, M.,  
989 Yebra, M., & Riaño, D. (2019). Estimación de variables esenciales de la vegetación en un ecosistema de

- 990 dehesa utilizando factores de reflectividad simulados con PROSAIL + FLIGHT. In A.E.d.  
991 Teledetección (Ed.), *XVIII Congreso Nacional de Teledetección*. Valladolid, Spain, 24-27 September  
992 2019
- 993 Martini, D., Pacheco-Labrador, J., Perez-Priego, O., van der Tol, C., El-Madany, S.T., Julitta, T.,  
994 Rossini, M., Reichstein, M., Christiansen, R., Rascher, U., Moreno, G., Martín, P.M., Yang, P., Carrara,  
995 A., Guan, J., González-Cascón, R., & Migliavacca, M. (2019). Nitrogen and Phosphorus Effect on Sun-  
996 Induced Fluorescence and Gross Primary Productivity in Mediterranean Grassland. *Remote Sensing*, *11*
- 997 McKay, M.D., Beckman, R.J., & Conover, W.J. (1979). A Comparison of Three Methods for Selecting  
998 Values of Input Variables in the Analysis of Output from a Computer Code. *Technometrics*, *21*, 239-  
999 245
- 1000 Melendo-Vega, J., Martín, M., Pacheco-Labrador, J., González-Cascón, R., Moreno, G., Pérez, F.,  
1001 Migliavacca, M., García, M., North, P., & Riaño, D. (2018). Improving the Performance of 3-D  
1002 Radiative Transfer Model FLIGHT to Simulate Optical Properties of a Tree-Grass Ecosystem. *Remote*  
1003 *Sensing*, *10*, 2061
- 1004 Migliavacca, M., Galvagno, M., Cremonese, E., Rossini, M., Meroni, M., Sonnentag, O., Cogliati, S.,  
1005 Manca, G., Diotri, F., Busetto, L., Cescatti, A., Colombo, R., Fava, F., Morra di Cella, U., Pari, E.,  
1006 Siniscalco, C., & Richardson, A.D. (2011). Using digital repeat photography and eddy covariance data  
1007 to model grassland phenology and photosynthetic CO<sub>2</sub> uptake. *Agricultural and Forest Meteorology*,  
1008 *151*, 1325-1337
- 1009 Migliavacca, M., Perez-Priego, O., Rossini, M., El-Madany, T.S., Moreno, G., van der Tol, C., Rascher,  
1010 U., Berninger, A., Bessenbacher, V., Burkart, A., Carrara, A., Fava, F., Guan, J.-H., Hammer, T.W.,  
1011 Henkel, K., Juarez-Alcalde, E., Julitta, T., Kolle, O., Martín, M.P., Musavi, T., Pacheco-Labrador, J.,  
1012 Pérez-Burgueño, A., Wutzler, T., Zaehle, S., & Reichstein, M. (2017). Plant functional traits and  
1013 canopy structure control the relationship between photosynthetic CO<sub>2</sub> uptake and far-red sun-induced  
1014 fluorescence in a Mediterranean grassland under different nutrient availability. *New Phytologist*, *214*,  
1015 1078-1091
- 1016 Omlin, M., & Reichert, P. (1999). A comparison of techniques for the estimation of model prediction  
1017 uncertainty. *Ecological Modelling*, *115*, 45-59
- 1018 Pacheco-Labrador, J., El-Madany, T., Martín, M., Migliavacca, M., Rossini, M., Carrara, A., & Zarco-  
1019 Tejada, P.J. (2017). Spatio-Temporal Relationships between Optical Information and Carbon Fluxes in  
1020 a Mediterranean Tree-Grass Ecosystem. *Remote Sensing*, *9*, 608
- 1021 Pacheco-Labrador, J., Perez-Priego, O., El-Madany, T.S., Julitta, T., Rossini, M., Guan, J., Moreno, G.,  
1022 Carvalhais, N., Martín, M.P., Gonzalez-Cascon, R., Kolle, O., Reischtein, M., van der Tol, C., Carrara,  
1023 A., Martini, D., Hammer, T.W., Moossen, H., & Migliavacca, M. (2019). Multiple-constraint inversion  
1024 of SCOPE. Evaluating the potential of GPP and SIF for the retrieval of plant functional traits. *Remote*  
1025 *Sensing of Environment*, *234*, 111362

- 1026 Perez-Priego, O., El-Madany, T.S., Migliavacca, M., Kowalski, A.S., Jung, M., Carrara, A., Kolle, O.,  
1027 Martín, M.P., Pacheco-Labrador, J., Moreno, G., & Reichstein, M. (2017). Evaluation of eddy  
1028 covariance latent heat fluxes with independent lysimeter and sapflow estimates in a Mediterranean  
1029 savannah ecosystem. *Agricultural and Forest Meteorology*, 236, 87-99
- 1030 Perez-Priego, O., Guan, J., Rossini, M., Fava, F., Wutzler, T., Moreno, G., Carvalhais, N., Carrara, A.,  
1031 Kolle, O., Julitta, T., Schrumpp, M., Reichstein, M., & Migliavacca, M. (2015). Sun-induced  
1032 chlorophyll fluorescence and photochemical reflectance index improve remote-sensing gross primary  
1033 production estimates under varying nutrient availability in a typical Mediterranean savanna ecosystem.  
1034 *Biogeosciences*, 12, 6351-6367
- 1035 Porcar-Castell, A., Tyystjärvi, E., Atherton, J., van der Tol, C., Flexas, J., Pfündel, E.E., Moreno, J.,  
1036 Frankenberg, C., & Berry, J.A. (2014). Linking chlorophyll a fluorescence to photosynthesis for remote  
1037 sensing applications: mechanisms and challenges. *Journal of Experimental Botany*, 65, 4065-4095
- 1038 Pourcel, L., Routaboul, J.-M., Cheynier, V., Lepiniec, L., & Debeaujon, I. (2007). Flavonoid oxidation  
1039 in plants: from biochemical properties to physiological functions. *Trends in Plant Science*, 12, 29-36
- 1040 Ren, H., & Zhang, B. (2018). Spatiotemporal variations in litter mass and their relationships with  
1041 climate in temperate grassland: A case study from Xilingol grassland, Inner Mongolia (China).  
1042 *Advances in Space Research*, 61, 1055-1065
- 1043 Richardson, A.D., Keenan, T.F., Migliavacca, M., Ryu, Y., Sonnentag, O., & Toomey, M. (2013).  
1044 Climate change, phenology, and phenological control of vegetation feedbacks to the climate system.  
1045 *Agricultural and Forest Meteorology*, 169, 156-173
- 1046 Rogers, A. (2014). The use and misuse of  $V_{c,max}$  in Earth System Models. *Photosynthesis Research*,  
1047 119, 15-29
- 1048 Rogers, A., Medlyn Belinda, E., Dukes Jeffrey, S., Bonan, G., Caemmerer, S., Dietze Michael, C.,  
1049 Kattge, J., Leakey Andrew, D.B., Mercado Lina, M., Niinemets, Ü., Prentice, I.C., Serbin Shawn, P.,  
1050 Sitch, S., Way Danielle, A., & Zaehle, S. (2016). A roadmap for improving the representation of  
1051 photosynthesis in Earth system models. *New Phytologist*, 213, 22-42
- 1052 Rouse, J.W., Haas, R.H., Schell, J.A., & Deering, D.W. (1974). Monitoring vegetation systems in the  
1053 Great Plains with ERTS. In S.C. Freden, E.P. Mercanti, & M.A. Becker (Eds.), *Third Earth Resources*  
1054 *Technology Satellite- 1 Symposium* (pp. 301-317). Greenbelt, MD, USA: NASA
- 1055 Sanaullah, M., Chabbi, A., Lemaire, G., Charrier, X., & Rumpel, C. (2010). How does plant leaf  
1056 senescence of grassland species influence decomposition kinetics and litter compounds dynamics?  
1057 *Nutrient Cycling in Agroecosystems*, 88, 159-171
- 1058 Schaefer, K., Schwalm Christopher, R., Williams, C., Arain, M.A., Barr, A., Chen Jing, M., Davis  
1059 Kenneth, J., Dimitrov, D., Hilton Timothy, W., Hollinger David, Y., Humphreys, E., Poulter, B.,  
1060 Raczka Brett, M., Richardson Andrew, D., Sahoo, A., Thornton, P., Vargas, R., Verbeeck, H.,  
1061 Anderson, R., Baker, I., Black, T.A., Bolstad, P., Chen, J., Curtis Peter, S., Desai Ankur, R., Dietze, M.,  
1062 Dragoni, D., Gough, C., Grant Robert, F., Gu, L., Jain, A., Kucharik, C., Law, B., Liu, S., Lokipitiya,



- 1063 E., Margolis Hank, A., Matamala, R., McCaughey, J.H., Monson, R., Munger, J.W., Oechel, W., Peng,  
1064 C., Price David, T., Ricciuto, D., Riley William, J., Roulet, N., Tian, H., Tonitto, C., Torn, M., Weng,  
1065 E., & Zhou, X. (2012). A model-data comparison of gross primary productivity: Results from the North  
1066 American Carbon Program site synthesis. *Journal of Geophysical Research: Biogeosciences*, 117
- 1067 Serbin, S.P., Singh, A., Desai, A.R., Dubois, S.G., Jablonski, A.D., Kingdon, C.C., Kruger, E.L., &  
1068 Townsend, P.A. (2015). Remotely estimating photosynthetic capacity, and its response to temperature,  
1069 in vegetation canopies using imaging spectroscopy. *Remote Sensing of Environment*, 167, 78-87
- 1070 Silva-Perez, V., Molero, G., Serbin, S.P., Condon, A.G., Reynolds, M.P., Furbank, R.T., & Evans, J.R.  
1071 (2018). Hyperspectral reflectance as a tool to measure biochemical and physiological traits in wheat.  
1072 *Journal of Experimental Botany*, 69, 483-496
- 1073 Sims, D.A., & Gamon, J.A. (2002). Relationships between leaf pigment content and spectral reflectance  
1074 across a wide range of species, leaf structures and developmental stages. *Remote Sensing of*  
1075 *Environment*, 81, 337-354
- 1076 Taranto, F., Pasqualone, A., Mangini, G., Tripodi, P., Miazzi, M.M., Pavan, S., & Montemurro, C.  
1077 (2017). Polyphenol Oxidases in Crops: Biochemical, Physiological and Genetic Aspects. *International*  
1078 *Journal of Molecular Sciences*, 18, 377
- 1079 van der Tol, C., Rossini, M., Cogliati, S., Verhoef, W., Colombo, R., Rascher, U., & Mohammed, G.  
1080 (2016). A model and measurement comparison of diurnal cycles of sun-induced chlorophyll  
1081 fluorescence of crops. *Remote Sensing of Environment*, 186, 663-677
- 1082 van der Tol, C., Verhoef, W., Timmermans, J., Verhoef, A., & Su, Z. (2009). An integrated model of  
1083 soil-canopy spectral radiances, photosynthesis, fluorescence, temperature and energy balance.  
1084 *Biogeosciences*, 6, 3109-3129
- 1085 Verhoef, W. (1984). Light scattering by leaf layers with application to canopy reflectance modeling:  
1086 The SAIL model. *Remote Sensing of Environment*, 16, 125-141
- 1087 Verhoef, W., & Bach, H. (2003). Remote sensing data assimilation using coupled radiative transfer  
1088 models. *Physics and Chemistry of the Earth, Parts A/B/C*, 28, 3-13
- 1089 Verhoef, W., van der Tol, C., & Middleton, E.M. (2018). Hyperspectral radiative transfer modeling to  
1090 explore the combined retrieval of biophysical parameters and canopy fluorescence from FLEX –  
1091 Sentinel-3 tandem mission multi-sensor data. *Remote Sensing of Environment*, 204, 942-963
- 1092 Vilfan, N., van der Tol, C., Muller, O., Rascher, U., & Verhoef, W. (2016). Fluspect-B: A model for  
1093 leaf fluorescence, reflectance and transmittance spectra. *Remote Sensing of Environment*, 186, 596-615
- 1094 Vilfan, N., Van der Tol, C., Yang, P., Wyber, R., Malenovský, Z., Robinson, S.A., & Verhoef, W.  
1095 (2018). Extending Fluspect to simulate xanthophyll driven leaf reflectance dynamics. *Remote Sensing of*  
1096 *Environment*, 211, 345-356

- 1097 Wang, Q., Tenhunen, J., Dinh, N.Q., Reichstein, M., Otieno, D., Granier, A., & Pilegarrrd, K. (2005).  
1098 Evaluation of seasonal variation of MODIS derived leaf area index at two European deciduous  
1099 broadleaf forest sites. *Remote Sensing of Environment*, 96, 475-484
- 1100 Wenhan, Q. (1993). Modeling bidirectional reflectance of multicomponent vegetation canopies. *Remote*  
1101 *Sensing of Environment*, 46, 235-245
- 1102 Whitfield, D.M., & Rowan, K.S. (1974). Changes in the chlorophylls and carotenoids of leaves of  
1103 *Nicotiana tabacum* during senescence. *Phytochemistry*, 13, 77-83
- 1104 Yang, P., Verhoef, W., & van der Tol, C. (2017). The mSCOPE model: A simple adaptation to the  
1105 SCOPE model to describe reflectance, fluorescence and photosynthesis of vertically  
1106 heterogeneous canopies. *Remote Sensing of Environment*, 201, 1-11
- 1107 Yuan, Z., & Chen, H.Y.H. (2009). Global trends in senesced-leaf nitrogen and phosphorus. *Global*  
1108 *Ecology and Biogeography*, 18, 532-542
- 1109 Zhang, Y., Guanter, L., Berry Joseph, A., Joiner, J., Tol, C., Huete, A., Gitelson, A., Voigt, M., &  
1110 Köhler, P. (2014). Estimation of vegetation photosynthetic capacity from space-based measurements of  
1111 chlorophyll fluorescence for terrestrial biosphere models. *Global Change Biology*, 20, 3727-3742
- 1112 Zhang, Y., Guanter, L., Joiner, J., Song, L., & Guan, K. (2018). Spatially-explicit monitoring of crop  
1113 photosynthetic capacity through the use of space-based chlorophyll fluorescence data. *Remote Sensing*  
1114 *of Environment*, 210, 362-374
- 1115